

Key Points:

- Characterizing free-floating mineral and soybean oil spills through integration of drift simulations, remote sensing, and in situ data
- Dynamics of oil spill extent and its evolution over time are accurately resolved by numerical modeling
- For thin oil films, optical and radar imagery show different detection capabilities

Correspondence to:

C. Brekke,
camilla.brekke@uit.no

Citation:




Brekke, C., Espeseth, M. M., Dagestad, K.-F., Röhrs, J., Hole, L. R., & Reigber, A. (2021). Integrated analysis of multisensor datasets and oil drift simulations—a free-floating oil experiment in the open ocean. *Journal of Geophysical Research: Oceans*, 126, e2020JC016499. <https://doi.org/10.1029/2020JC016499>

Received 29 JUN 2020
 Accepted 6 NOV 2020

© 2020. The Authors.

This is an open access article under the terms of the Creative Commons Attribution-NonCommercial-NoDerivs License, which permits use and distribution in any medium, provided the original work is properly cited, the use is non-commercial and no modifications or adaptations are made.

Integrated Analysis of Multisensor Datasets and Oil Drift Simulations—A Free-Floating Oil Experiment in the Open Ocean

Camilla Brekke¹ , Martine M. Espeseth¹, Knut-Frode Dagestad² , Johannes Röhrs² , Lars Robert Hole², and Andreas Reigber³

¹UiT The Arctic University of Norway, Tromsø, Norway, ²The Norwegian Meteorological Institute, Oslo, Norway, ³DLR, Microwaves and Radar Institute, Oberpfaffenhofen-Wessling, Germany

Abstract A free-floating oil spill experiment (two oil types) in the open ocean is described, and the results from slick characterization through integrated analysis of drift simulations with remote sensing and in situ data are discussed. We compare oil drift simulations (OpenOil), applying various configurations of wind, wave, and current information, with the observed slick positions and shape. We describe trajectories and dynamics of the spills, slick extent, and their evolution, and the differences in detection capabilities in optical instruments versus multifrequency PolSAR acquired by Deutsches Zentrum für Luft-und Raumfahrt F-SAR. When using the best available forcing from in situ data and forecast models, good agreement with the observed position and extent was found. A fair agreement is obtained using only numerical forecast data as input. This case study reveals that the accuracy when using modeled current is relatively higher after one full local inertial period, as the effect of incorrectly modeled amplitude of the inertial current is then vanishing. This should be a general result applicable to any oceanic drift forecast based on the modeled current. A novelty is the comparison of viscous-similar soybean and mineral oil. Our findings indicate that biological oil emulsions potentially could replace mineral oil emulsions in contingency and rehearsal campaigns, but this finding is only supported from an oil drift prediction perspective. Differences in mineral oil detection capabilities are found between synthetic aperture radar and optical imagery of thinner sheen regions. F-SAR appears to be more sensitive to thinner oil and detect a larger extent, and differences between the thinner and thicker parts are observed.

Plain Language Summary The scientific results presented in this paper are of relevance for agencies providing and using oil spill monitoring services and organizations engaged in oil spill contingency and preparedness planning. In particular, we present the results from a free-floating oil spill experiment in the open ocean. We look at ways in which to characterize mineral and soybean oil spills through integration of oil drift simulations, data collected from imaging sensors in air and space, and data collected locally on-site. The results document that it is possible to obtain good agreement between predicted drift and observations. Our findings indicate that biological oil potentially could replace mineral oil in oil spill contingency and rehearsal campaigns, but this result is only supported when the purpose is to study oil spill monitoring and trajectory simulations. This study also reveals differences in oil detection capabilities between the different sensors studied.

1. Introduction

Recent effort has gone into investigating the oil slick characterization capabilities of emerging radar sensors and drift simulations. Oil slick characterization involves problems such as separating mineral oil spills from look-alikes, for example, natural low-radar backscatter phenomena, extraction of physical oil properties such as the dielectric constant of the medium, estimating relative slick thickness, the oil volumetric fraction of an oil/water emulsion, and, finally, predicting slick drift and evolution. This work describes the experimental setup and results from a thoroughly planned and successfully conducted oil spill field campaign that took place in the North Sea in June 2019 as a part of the Norwegian Clean Seas Association for Operating Companies (NOFOS) annual oil-on-water exercise.

Brekke and Jones (2020) give an overview of the key information items pertaining to marine oil pollution surveillance, response, remediation, and preparedness involving the synthetic aperture radar (SAR). During the tactical clean-up stage of an oil spill incident, information about zones of relatively larger thickness and drift and spread predictions are examples of key items. Studies investigating oil spill characterization (see Minchew et al., 2012; Skrunes et al., 2014) using SAR have shown various successes, with the most promising results when the SAR sensor is mounted on an airplane with low noise floor and fine spatial and temporal resolution (see Minchew et al., 2012). The frequency choice of the imaging radar is an important parameter when characterizing marine oil pollution by SAR. True multifrequency SAR datasets of oil spills are rarely described in the literature. Hühnerfuss et al. (1996, 1994) describe oil spill experiments using the multifrequency instrument HELISCAT (Ku-, X-, C-, S-, and L-bands) that was attached on a helicopter flying over different types of artificial surface films in 1990, 1992, and 1993. Furthermore, in 1994 the spaceshuttle Endeavor carried the multifrequency instrument named SIR-C/X-SAR (X-, C-, and L-band) and imaged three different controlled slick experiments around the world (Gade et al., 1998). We present a unique time series of simultaneous quad-polarimetric multifrequency X-, S-, and L-band SAR imagery with fine resolution, and two oil emulsion types are investigated in this study: soybean and mineral oil. A uniqueness of this experiment, making it stand out from previous experiments (Hühnerfuss et al., 1994, 1996; Skrunes et al., 2016), lies in the combination of optical data and in situ measurements acquired close in time with the SAR imagery.

Oil spill characterization has also been performed using optical instruments. For some tasks, optical sensors have shown more promising potential than SAR, given specific met-ocean and sun conditions (see Fingas & Brown, 2014). The Bonn Agreement Oil Appearance Code (BAOAC) (Bonn Agreement, 2016), applied to optical imagery and the use of infrared (IR) sensors, has demonstrated that information about relative oil slick thickness can be extracted. Differences in areal detection capabilities are observed between radar acquisitions and optical acquisitions of the free-floating oil slicks. Radar and optical remote sensing have been applied in previous oil spill measurements (see Liu et al., 2011). However, most of the studies involving SAR and optical have been performed separately, not allowing a direct comparison and investigation of their combined use. Our data set contains a unique collection of close-in-time radar (aircraft and satellite) and optical measurements (aircraft, aerostat, and drone) of the slicks. This provides an opportunity to do a thorough comparison of the characteristics of mineral oil slicks in SAR imagery versus their appearance in optical imagery, including area extent.

We furthermore collected in situ wind and current measurements to address the surface and subsurface drift and slick extent. A realistic description of the oil spill area extent in simulations is needed to achieve a synthesis between remote sensing and modeling of spills. Modeling of the spill area extent relies on physical processes that change the spill area and vertical extent, and presently there exist various explanations for oil spill spreading. Elliott (1986) suggests that vertical shear and differences in forcing between the surface and submerged oil lead to a protrusion of downwind extent. Simecek-Beatty and Lehr (2017) suggest that Langmuir circulation plays a major role for creating downwind streaks of oil spills. Most likely, a combination of various mechanisms is at play. Time series of remote sensing images together with observations of in situ environmental conditions can address the spreading of surface slicks in more detail, as performed in Jones et al. (2016) and this study. As such, carefully controlled campaigns where both the oil release and environmental conditions are known in great detail are very rare; it is of utmost importance to extract as much knowledge as possible from the data. This should be done in order to establish or verify existing drift model parameterizations, which are to a large degree based on laboratory measurements. We focus here on the first few hours after the spill when uncontrolled factors are minimized, in comparison to, for example, the Deepwater Horizon accident, where the large temporal and spatial scales, combined with a release at the seafloor, involved more uncertainties (Liu et al., 2011). Precise reproduction and modeling of the initial phase of an oil spill should be a prerequisite for successful long-term prediction.

Biogenic slicks originating from, for example, algae or fish oil is the cause of many false alarms in remote sensing oil spill services, hampering the accuracy of the information about man-made pollution delivered to customers such as contingency preparedness and coastal monitoring agencies. This has been one of the driving forces to apply plant oil in addition to mineral oil types in large-scale experiments and rehearsal exercises in Norway, where remote sensing data from satellite and aircraft have been collected. However,

whether the plant oil type previously applied is a viable proxy for natural biogenic slicks is a topic of discussion. During the NOFO oil-on-water exercises from 2011 to 2015, Radiagreen EBO plant oil was released as a biogenic slick simulator. In previous works (e.g., Espeseth et al., 2017; Skrunes et al., 2014), the plant oil slicks were used as reference oil spills for comparison with true mineral oil spills in multipolarization SAR imagery. In oil drift simulations, plant oil and mineral oil have been distinguished by their median droplet size to reflect the differences in their respective drift behavior (Jones et al., 2016). Based on realistic descriptions of the oil droplet size spectra, Johansen et al. (2015), Li et al. (2017), and Röhrs et al. (2018) showed that vertical mixing processes control the differences in horizontal transport of various oil types and in various weather conditions; however, the study scope was limited to mineral oil emulsions.

A novel part of this study is a comparison of the viscous-similar soybean oil and mineral oil emulsions with regard to remote sensing and modeling. The choice to include a sustainable oil type in this work is motivated by a request for *greener* substances to apply in oil spill preparedness exercises, assuming small spills and where the wildlife is still taken into consideration. Oil spill preparedness agencies are seeking to find a more environmentally friendly substance that could act as a substitute for real mineral oil during equipment rehearsals. In this work, we investigate whether soybean oil emulsion could work as a suitable substitute for mineral oil emulsion for agencies training in the marine environment. We look at the problem from both a multisensor remote sensing and oil drift simulation perspective, but do not investigate the actual impact of soybean oil on the marine wildlife.

For the convenience of the reader, we summarize the topics addressed in this work as follows:

- Soybean versus mineral oil emulsions comparison by remote sensing and modeling;
- Oil-to-sea contrast in multifrequency SAR imagery;
- Remotely sensed temporal evolution of oil slick extent;
- Modeled oil distribution and trajectory versus observed position and extent;
- Met-ocean forcing options and physical oil droplet parameterization in the model;
- Slick evolution and appearance in optical versus SAR imagery.

The layout of this study is as follows: Section 2 describes the experimental setup. The methodology applied to segment out the slicks from remote sensing data is described in Section 3, along with a discussion of the observed evolution in area extent of the mineral and soybean oil slicks. Section 4 presents the open-source oil drift model applied in this work. The slick segments are used in Section 5 for a comparison with oil slick drift simulations. In Section 6, pairs of optical and SAR imagery are investigated with respect to mineral oil slick characterization. Finally, Section 7 draws the conclusions and we give some future outlook.

2. Experimental Setup

The Norwegian Radar oil Spill Experiment (NORSE2019) was conducted in the North Sea in June 2019 as a part of NOFOs annual oil-on-water exercise. By integrating NORSE2019 in NOFOs annual exercise, the scientific efforts described in this paper could leverage their infrastructure, expertise, and well-established framework for environmentally precautionous operations. Figure 1 presents a map identifying the study site.

The analysis presented is confined to the data set acquired on June 12, the main day of the NORSE2019 experiment. Figure 2 illustrates a timeline of the remote sensing activities from air and space and in situ measurements in the water between 03:14UTC and 20:20UTC. The airborne and spaceborne remote sensing activities are indicated above the blue line, whereas activities on and under the sea surface are shown below this line. 2 m³ mineral oil emulsion was first released followed by 2 m³ soybean oil emulsion. The oil releases and properties of the substances are described in more detail in Section 2.1.

At and below the sea surface, several different in situ measurements were collected. An autonomous sail buoy was deployed prior to the release of the two oil types to measure the weather conditions near the sea surface. During the release of the mineral oil, three different passive surface drifters were deployed (drifter set 1) to sample the surface drift currents at various depths. In conjunction with the soybean oil emulsion release, the same three passive surface drifters were also released (drifter set 2). More information about the in situ measurements are further described in Section 2.2.

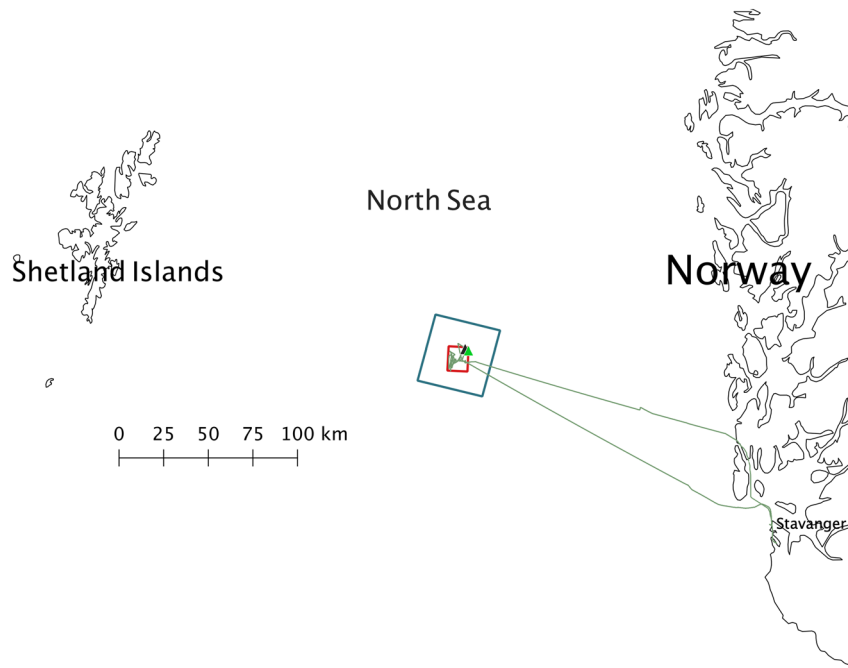


Figure 1. NOFO's oil-on-water 2019 exercise field (blue box) in the North Sea. The majority of the NORSE2019 activities took place in the red box on June 12. The black and green triangles represent the release positions of mineral and soybean oil emulsions, respectively. The green line is the ship track of research vessel Helmer Hanssen (RV HH), outbound from Stavanger (southern green line) on June 11. NOFO's, Norwegian Clean Seas Association for Operating Companies; NORSE2019, Norwegian Radar oil Spill Experiment.

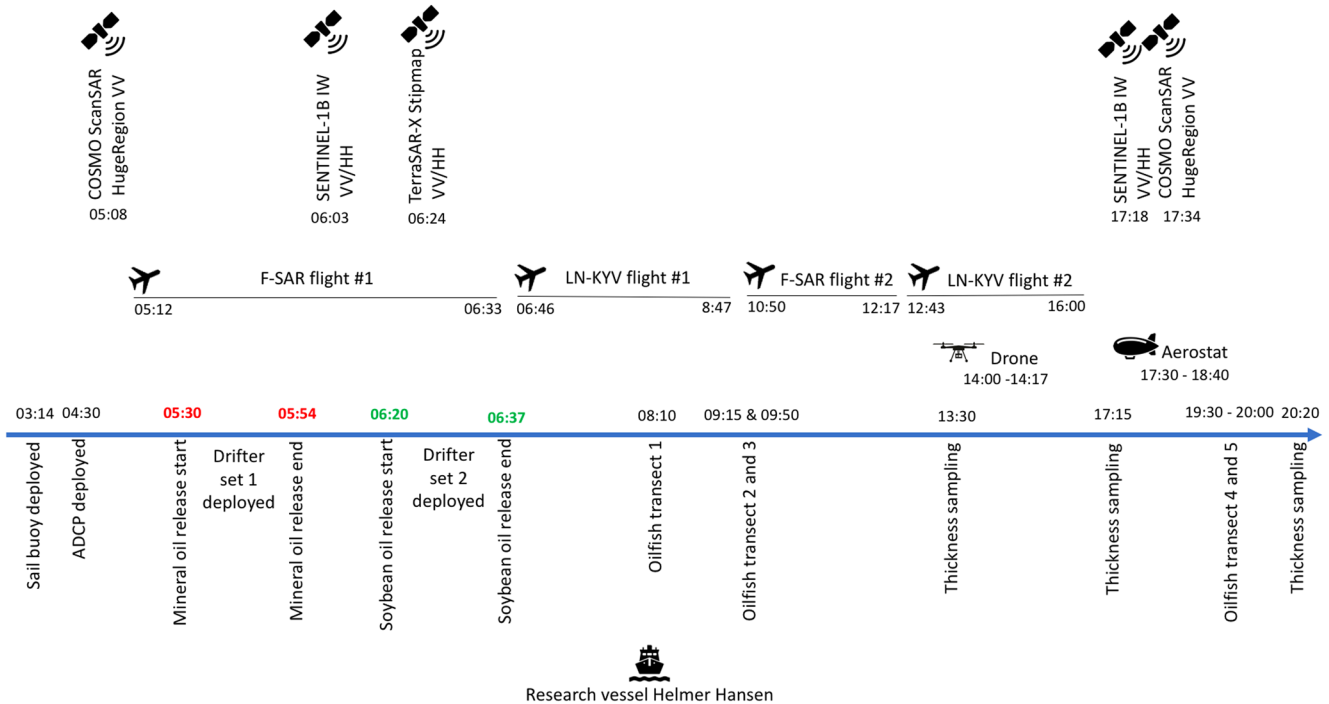


Figure 2. Graphic view of the NORSE2019 June 12 timeline. All timestamps are in UTC. The blue line represents time on nonlinear scale as well as the air-water interface. Red (green) time stamps indicate release start and stop of mineral (soybean) oil emulsion. The sets of drifters contained both surface current drifters as well as positioning drifters. More details about the drifters are given in Table 2. NORSE2019, Norwegian Radar oil Spill Experiment.

Table 1
Composition of the Emulsions, Viscosity, and Amount of Substances at Release

Type	Composition	Viscosity	Volume
		(mPa · s)	(m ³)
Mineral oil emulsion	45% oil (10 parts evaporated ^a Oseberg Blend and 1 part IF 380) and 55% seawater	1,500–1,600	2
Biogenic oil emulsion	33% soybean oil and 67% seawater	1,700–1,800	2

^aResidue after evaporation.

In the air, we had one aircraft from Deutsches Zentrum für Luft-und Raumfahrt (DLR) dedicated to the NORSE2019 experiment. This aircraft was carrying the F-SAR instrument as payload (see Horn et al., 2009) for more information regarding the F-SAR instrument). The planning of these flights was done as a collaborative effort between DLR, UiT, The Arctic University of Norway, and NOFO. In addition, the LN-KYV aircraft from the Norwegian Coastal Administration (NCA) was involved with NOFO in the oil-on-water exercise, and interleaved with the DLR aircraft over the site and NORSE2019 activities (Figure 2). We had also a drone and an aerostat in the air, both operated from the research vessel Helmer Hanssen (RV HH). Finally, from space, we had satellite SAR acquisitions from the Sentinel-1B, TerraSAR-X, and COSMO-SkyMed missions. From the spaceborne imagery, only oil spill segments or masks are used, while the airborne data is investigated in more depth. For a complete description of the experiment, both the airborne and spaceborne remote sensing acquisitions are further described in Section 2.3.

2.1. Oil Releases

The RV HH took part in the experiment, leaving for the study site 11 June and returning back to Stavanger (indicated on the map in Figure 1) on June 14, 2019. NOFO released the two oil emulsions from the vessel, and the composition and mixing of the oil emulsions were done by NOFO personnel (Engen et al., 2019). Table 1 gives an overview of the substances applied. Figure 3 shows a close-up view of the mineral oil spill about 13 h after release and the soybean oil spill at release. The visual appearance of the two substances is evidently different. In the left panel, with the wind speed gradually picking up from around noon, white caps due to wave breaking are visible on the ocean surface.

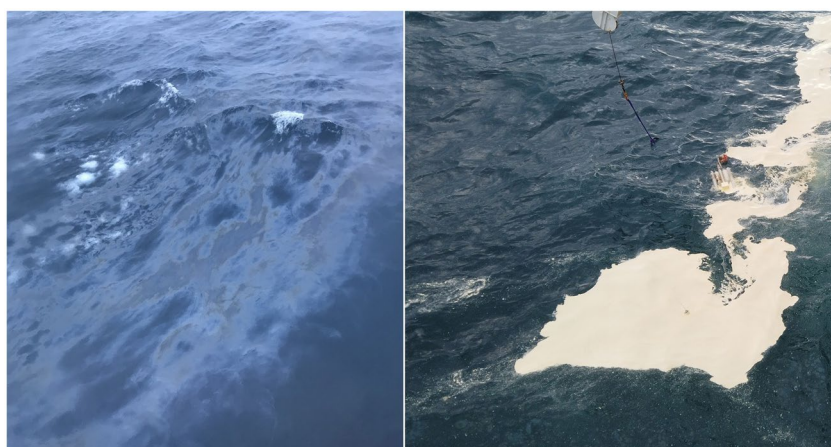


Figure 3. Left: Close-up view of the mineral oil emulsion spill taken from RV HH June 12 at 20:20UTC. Photo: Camilla Brekke. Right: Photo of the soybean oil emulsion spill at release taken from RV HH UTC June 12 at ~06:30UTC. Photo: A. Malin Johansson. Photos published with permission from NOFO. Abbreviations: NOFO's, Norwegian Clean Seas Association for Operating Companies; RV HH, research vessel Helmer Hanssen.

Table 2
In situ Variable Collections Conducted From RV HH

Variable	Infrastructure	Responsible
Wind speed	SailBuoy	MET Norway
Wind direction		
Air temperature		
Current, surface	iSphere drifter	MET Norway
Current, 1-m depth	CODE drifter	MET Norway
Current, 15-m depth	SVP drifter	MET Norway
Current, surface	Osker drifter	Env. Canada
Georeferencing	AIS drifter	NOFO
Ocean current	ADCP	MET Norway
Directional wave spectra		
Subsurface oil particle concentration	Oilfish	CSIRO
Conductivity	CTD	CSIRO
Temperature		
Pressure of seawater		
Thickness	Oil sampler	Water mapping, LLC

Note. Thickness samples were only collected from the mineral oil emulsion. Data from the AIS drifter, ADCP, Oilfish, CTD, and oil sampler are not used in this study and are therefore left out in the following discussions, but included here for completeness and future reference about the campaign.

Abbreviations: ADCP, Acoustic Doppler Current Profiler; AIS, Automatic Identification System; CODE, Coastal Ocean Dynamics Experiment; CTD, Conductivity, Temperature and Depth; NOFO, Norwegian Clean Seas Association for Operating Companies; RV HH, research vessel Helmer Hanssen; SVP, Surface Velocity Program.

The mineral oil emulsion consisted of evaporated Oseberg Blend crude oil, that is, the remaining part after evaporation, and this oil type has been used in prior oil-on-water experiments in 2011–2013, 2015, 2016, and 2018. See, for example, Skrunes et al. (2014), Skrunes et al. (2015a, 2015b, 2017), Espeseth et al. (2017), Jones et al. (2016) for more detailed information about the experiments and the oil releases. During NORSE2019, the two oil slicks were freely floating, but in situ thickness sampling and transects from towing the Oilfish into the oil were performed multiple times from the ship (see Figure 2).

The releases of biogenic oil together with mineral oil have also been conducted previously in several oil-on-water experiments (2011–2013 and 2015), but then Radiagreen EBO was used (see Skrunes et al., 2014, 2017). Radiagreen EBO has much lower viscosity (about 7 mPas) than both mineral oil emulsion and crude oil (1,500–1,800 mPas) (Skrunes et al., 2015a), and studies have shown the possibility to discriminate the two (Skrunes et al., 2014). The damping of the short capillary ocean waves, responsible for the radar backscatter, is determined by the thickness of the oil layer and the varying viscosity of the oil (Alpers et al., 2017; Wismann et al., 1998), and viscosity is hence a key and indirect driver of oil-water contrast in a SAR image. In the NORSE2019 experiment, a biogenic oil emulsion of soybean oil was released, which has very similar viscosity to the mineral oil emulsion (Table 1). Therefore, separating the two might be challenging using radar measurements. However, a biogenic alternative that resembles mineral oil allows us to investigate the opportunity to use the soybean oil emulsion as a viable alternative to mineral oil emulsions for future exercises. A biogenic substitute for mineral oil will likely reduce the impact on the environment, which motivates this study.

2.2. In Situ Measurements and Forecast Models

Table 2 presents the variables collected in situ by instruments deployed from RV HH during NORSE2019. In addition to the data sources listed in the table, photos of the drifting oil slicks and the surrounding sea surface were taken by regular cameras from both the RV HH and the DLR aircraft. Some video material

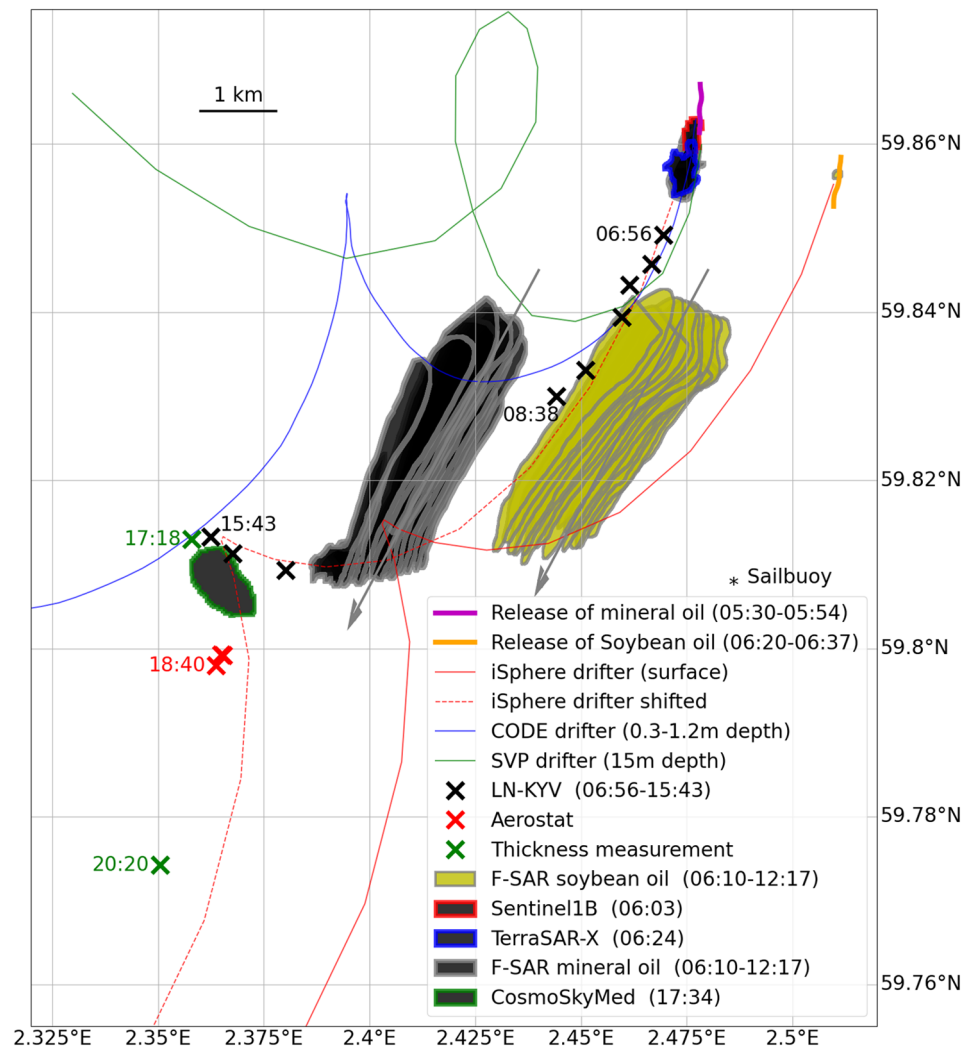


Figure 4. Overview of the release location and drift of the oil and drifters during June 12, 2019. The thick magenta and yellow line segments show the track of the ship during release of the mineral and soybean oils, respectively. The trajectory of a CODE drifter (0.6-m depth) and an SVP drifter (15-m depth) released together with the mineral oil are shown as blue and green lines, respectively. A surface drifter (iSphere) released together with the soybean oil is shown as a solid red line. The dashed red line shows the same trajectory, shifted to match the release location of the mineral oil. The black filled polygons show a time series of the mineral area oil as detected from satellites and airplane (F-SAR). The yellow polygons are the corresponding soybean oil area from F-SAR. Crosses show the center location of the mineral oil slick at various times throughout the day. Black crosses are based on aerial photographs from the LN-KYV airplane. Green crosses are selections of ship coordinates during sampling at the two (out of three) sites where in situ thickness measurements were made. The red crosses show the location of the oil slick based on aerial photos acquired from an Aerostat. Note that the F-SAR shows an elongated oil slick, whereas only the thickest, southernmost part (about 500 m) was visible by eye and satellites. Thus, the location of the crosses corresponds to the centroid of this southernmost part of the F-SAR polygons. The 2 gray arrows indicate the average wind direction (from 28° azimuth) from the start of the release until 12:00 UTC, as measured from the SailBuoy, whose location is indicated with an asterisk. The axes show the longitude and latitude in decimal degrees.

was also collected from the ship. The in situ measurements are compared with the corresponding modeled variables from the operational model suite at MET Norway, as presented in Table A1.

Figure 4 provides a georeferenced overview of the vessel positions at oil release, location of the F-SAR slick masks (evolving with time) and slick positioning from auxiliary data sources overlaid with the trajectories of the surface drifters, iSphere, CODE, and SVP. The three drifter types presented in Table 2 have various drift properties. The iSphere drifter is floating halfway submerged at the surface. This drifter is designed in

particular for oil spill tracking, and is affected by wind drag, waves, and surface currents (Röhrs et al., 2012). The CODE drifter follows surface currents at an effective depth of 0.6 m, due to a sail extending from 0.3 to 1.2 m depth, with little wind and wave drag (Davis, 1985), while the SVP is moved by currents at 15-m depth, which is the center of its 6-m long sail (“holey sock”). One triplet of current drifters (iSphere, CODE, and SVP) was released for each of the two spills, as indicated in Figure 2. The iSphere drifter of the first release (mineral oil) did not transmit any data. As for the similar campaign in Jones et al. (2016), the buoys of the same type showed coherently identical trajectories that were only shifted in space. Therefore, we show in Figure 4 only the CODE and SVP trajectories for the mineral oil spill, and only the iSphere for the soybean oil spill, as, respectively, blue, green, and red lines. The dashed red line shows the iSphere trajectory shifted in space to match with the release of the mineral oil.

The Offshore Sensing SailBuoy is a robust autonomous vessel which is 100% wind propelled. It has previously been used for a range of applications, including salinity and temperature measurements in the Gulf of Mexico (Ghani et al., 2014) and mid-winter directional wave measurements in the North Sea (Hole et al., 2016). In this application, it was supplied with an AirMar weather station and was stationary (heave to mode) in the vicinity of the spill location (Figure 4), mostly for near-surface wind measurements.

Ocean current data from the surface drifters and wind data from the SailBuoy are used as forcing in the oil drift simulations in Section 5. Near-surface currents are for this purpose retrieved from the CODE drifter that was released together with the mineral oil (Figure 4, blue line), using the same method as applied in Jones et al. (2016): the vector difference between two adjacent positions is divided by the time interval (here 10 min) to obtain the velocity vector. From this, the Stokes drift at the effective depth of the drifter (0.6 m) is subtracted, using surface Stokes drift from the wave model (Table A1), and a method outlined in Breivik et al. (2014).

Figure 5 shows the measured and modeled wind, waves, and currents during June 12 from 04UTC until midnight. The raw wind measurements from the ship (23 m above sea level, mast at the top of pilot house) were higher than the corresponding measurements from the SailBuoy at 0.5-m height (Figure 5a). However, very close agreement is obtained for wind calculated for 10-m height (Figure 5b), using the wind profile power law as follows:

$$U(z) = U_r(z / z_r)^{0.11} \quad (1)$$

where U_r is the measured wind at height z_r (Hsu et al., 1994).

The wind speed from the atmospheric forecast model (00UTC run, red line) is seen to be too low until 12UTC, then slightly too high until 18UTC, with better agreement with the observations in the evening. The wind direction (Figure 5c) is, however, in very good agreement between the model and the two measurements time series. Figure 5c also shows that the wave direction (including the Stokes drift direction) from the wave forecast model is almost directly from North, compared with the wind which has a north-easterly component, but no wave measurements were undertaken to verify this. Figure 5d shows the significant wave height from the wave model, about 2.6 m at the time of the oil releases, decreasing to 2.2 m around 14UTC, and again increasing to above 3 m in the evening when the wind increased. Figure 5e shows the surface current speed from the ocean forecast model (NorKyst), along with the corresponding drift current derived from the CODE drifter. For comparison of the relative importance to the oil drift, the modeled Stokes drift and the wind-induced surface current (2% of the model wind speed) are also shown. Figure 5f shows the air temperature with moderate variation through the day, and about 1.5° colder near the surface (SailBuoy) compared with the modeled temperature at 10 m and measured at 23 m (ship).

2.3. Remote Sensing Instruments

Table 3 gives an overview of the airborne remote sensing acquisitions, and Table B1 shows the sensor properties of the F-SAR instrument and the spaceborne acquisitions. Note that F-SAR records quad-polarimetric measurements. An analysis of radar polarimetry is, however, outside the scope of this paper and only the vertical on transmit/vertical on receive (VV) channel for any frequency is utilized here.

Two flights with F-SAR and two flights with LN-KYV were conducted. The flights were interleaved as only one airplane could be in the airspace above the site simultaneously. Both visible and IR photos/videos were

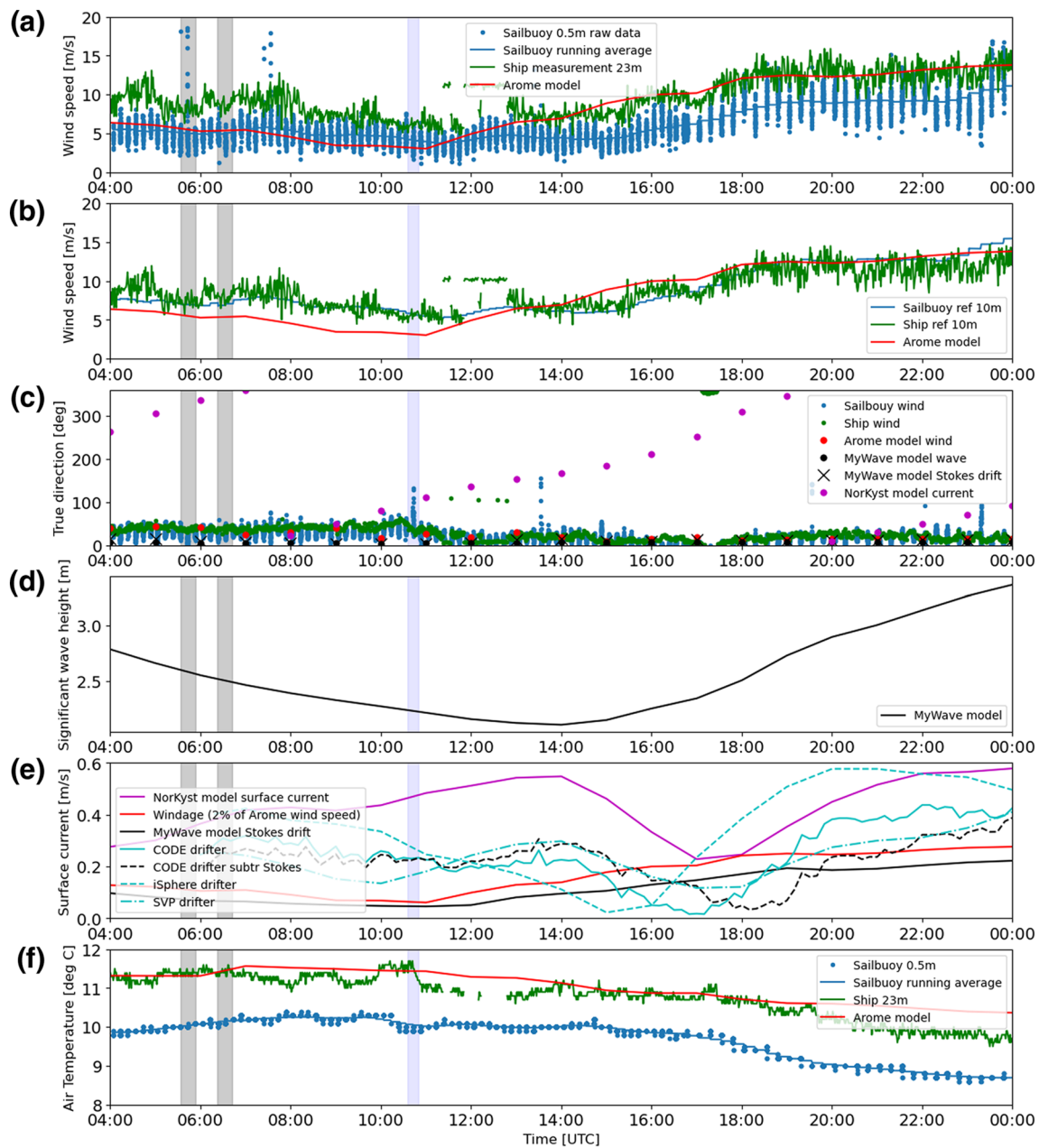


Figure 5. In situ measured (Table 2) and modeled (Table A1) wind, waves, and currents from June 12, 2019 04UTC until June 13, 2019 00UTC. The two vertical gray bars indicate the release times of the two oil spills. The vertical blue bar indicates a rain event. The subplots show from top to bottom: (a) raw wind measurements, (b) wind measurements corrected to 10-m height as described in the text, (c) directions of winds, waves, and currents (0 is from North, 90 is from east), (d) wave height from numerical model, (e) current speed, and (f) air temperature.

collected from LN-KYV, and visible (red, green, and blue [RGB]) images of the mineral oil and soybean oil slicks are shown in Figures 6 and 7, where the lower right panel in Figure 6 shows an aerostat image. The IR sensor on-board LN-KYV operates in the mid-infrared region (3–5 μm), that is, in the thermal infrared region. Throughout this study, only snapshots from the videos spanning several hours are displayed showing both the mineral and the soybean oil slicks.

At 06:56UTC, the mineral oil slick was confined to one slick with an elongated patch. At 13:04UTC, the mineral oil was fragmented into three parts. Later at 15:44UTC, more individual fragments are formed. It is evident that the mineral oil slick has changed its shape and extent since 06:56UTC (1 h after mineral oil

Table 3
Airborne Data Collections, June 12

Acquisition (Flight #)	Number of Scenes	Acquired [UTC]	Oil slicks captured, Ref. Table 1	Responsible
F-SAR (1)	12	05:12–06:33	Both, at start of release	DLR
F-SAR (2)	14	10:50–12:17	Both	
LN-KYV (1)	Video stream	06:55–08:39	Both	NOFO and NCA
LN-KYV (2)	Video stream	12:54–15:46	Both	
Drone flight	Video stream	14:00–14:17	Mineral oil emulsion	NORCE
Aerostat	Video stream	~18:15–18:40	Mineral oil emulsion	NOFO

Note. All F-SAR acquisitions are included in the timeframe indicated, whether they contain oil or no-oil. Abbreviations: DLR, Deutsches Zentrum für Luft-und Raumfahrt; NCA, Norwegian Coastal Administration; NOFO, Norwegian Clean Seas Association for Operating Companies;

release) and over the following several hours, due to spreading, weathering, and mixing. The soybean oil has also changed between 07:05UTC (30 min after release) and 12:54UTC (the last optical image available). At 07:05UTC, one can observe white patches (near the cross in the image, and not to be confused with white-capping) indicating thicker parts of the soybean oil slick. At 12:54, the white patches are not present any more. The reason may be that seabirds were observed feeding on the soybean slicks (Engen et al., 2019), though dispersion by waves may also have contributed. The remains after the intervention of the birds are most likely thinner parts of the soybean oil, which can be observed in the right image of Figure 7. The impact of the soybean oil on the seabirds is unknown (Engen et al., 2019), and this ecological issue should be investigated before any firm recommendation can be made on the applicability of soybean oil.

From visual inspection between the slick evolution of the mineral oil and soybean oil in Figures 6 and 7 (and additional video material not shown here), we see that the overall drift and extent of the slicks is very similar, although there are clear differences in the signatures within the slicks. If the difference is solely due to differences in oil composition at release, or if the interaction with seabirds (which is only the case for soybean oil) plays a larger role, is unknown. The soybean oil slick (at 12:54UTC) appears more homogeneous and exhibiting one color as opposed to the mineral oil slicks, which have patches of different colors (silver and brown) that indicate different oil thicknesses (according to the BAOAC [Bonn Agreement, 2016]). However, some similarities can be drawn from these optical time series, as both the mineral oil and the soybean oil slick (at 12:54UTC) have a brighter appearance than the clean sea.

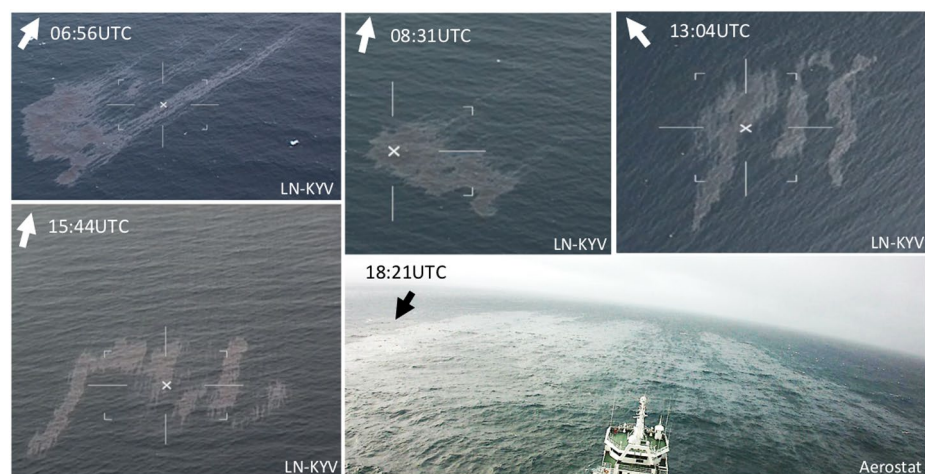


Figure 6. Snapshots (RGB images) from videos acquired with the LN-KYV and aerostat (tethered to RV HH) of the mineral oil slicks. The arrow indicates the north direction. Images published with permission from NOFO. NOFO, Norwegian Clean Seas Association for Operating Companies; RGB, red, green, and blue; RV HH, research vessel Helmer Hanssen.

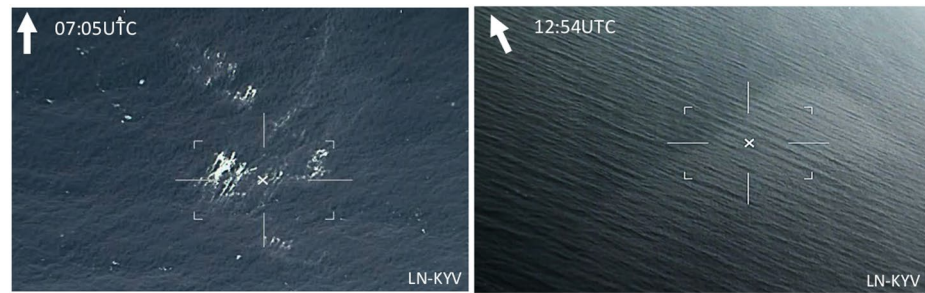


Figure 7. Snapshots (RGB images) from videos acquired with the LN-KYV of the soybean oil slicks. The arrow indicates the north direction. Images published with permission from NOFO. NOFO, Norwegian Clean Seas Association for Operating Companies; RGB, red, green, and blue.

A selection of VV-intensity images from the F-SAR time series are displayed in Figure 8, covering both the mineral oil and soybean oil slicks across several hours. The first, second, and third columns show VV-intensities from the X-, S-, and L-band sensors, respectively. The soybean oil was undergoing release in the images shown in the second row. Images from the second flight are shown from the third to the fifth rows, where the mineral oil is located above (northwest) the soybean oil slick. The availability of multifrequency SAR data covering oil slicks is limited, but similar oil spill experiments were conducted in the 1990s (Gade et al., 1998; Hühnerfuss et al., 1994, 1996). Gade et al. (1998) reported higher sea-oil contrast for X-band compared to L-band for mineral oil films, but stronger damping at L-band was reported for the biogenic (natural) surface slicks. Figures 8 and 9 show that the contrast between the mineral oil slicks and the surrounding clean sea is high at the X- and S-bands, and lower at the L-band. The same observation is made for the soybean oil slicks (see Figure 9). Similar oil damping at the C- and X-bands was also shown in Gade et al. (1998). Different fluctuations within the two oil slicks (see colored lines in Figure 9) are also seen across the three frequencies. Clearly, the frequency plays an important role with regard to the oil-sea contrast, differences between mineral oil and soybean oil, and internal differences that might indicate thickness variations. As seen in Table B1, the noise floor is very low for F-SAR compared with the spaceborne sensors. The noise floor is especially low for the L-band sensor followed by the S- and X-bands in the F-SAR. These low values might therefore allow for proper analysis of the backscattered signal from the oil for characterization purposes. Future work will be conducted regarding these topics, where the radiometry and signal-to-noise relationship of the F-SAR time series will be the focus. Additionally, a parallel study investigating a selection of F-SAR scenes will also soon be available. In this study, the focuses are slick transport, slick extent, and detection capabilities in SAR and optical imagery. As mentioned, variations are observed across the different frequencies used in SAR, but larger differences are seen between the optical (Figures 6 and 7) and microwave frequencies (Figure 8). Following this, Section 6 includes discussions and illustrations of the similarities and dissimilarities between the optical and F-SAR images shown in Figures 6–8.

3. Slick Segmentation

Two different sets of mineral oil masks are derived from the F-SAR time series using the S-band scenes, one representing the slick extent (oil vs. clean sea), and the other representing thick oil versus the rest of the oil. The oil mask of the entire slick is manually drawn from the VV-intensity of F-SAR (using S-band data), Sentinel-1, TerraSAR-X, and COSMO-SkyMed (by KSAT). This is performed on both the soybean and mineral oil slicks. The thickness oil masks from the S-band F-SAR scenes are only derived from the mineral oil, since such patches are not present within the soybean oil, which is homogeneous with an outer rim. The thickness oil masks are derived from an algorithm described in Doulgeris and Cristea (2018) and Cristea et al. (2020). The range of incidence angles in the F-SAR is wide (see Table B1) and the incidence-angle-induced intensity variations might be larger than the intensity difference between the classes, resulting in more classes based on the incidence angle rather than the relevant features like clean sea and oil. Hence, we use the statistical segmentation algorithm in Doulgeris and Cristea (2018) and Cristea et al. (2020), which adapts to the incidence angle gradient and uses a nonstationary Gaussian mixture model as input to an expectation-maximization (EM) algorithm. The inputs are the VV-intensity in decibel and the incidence

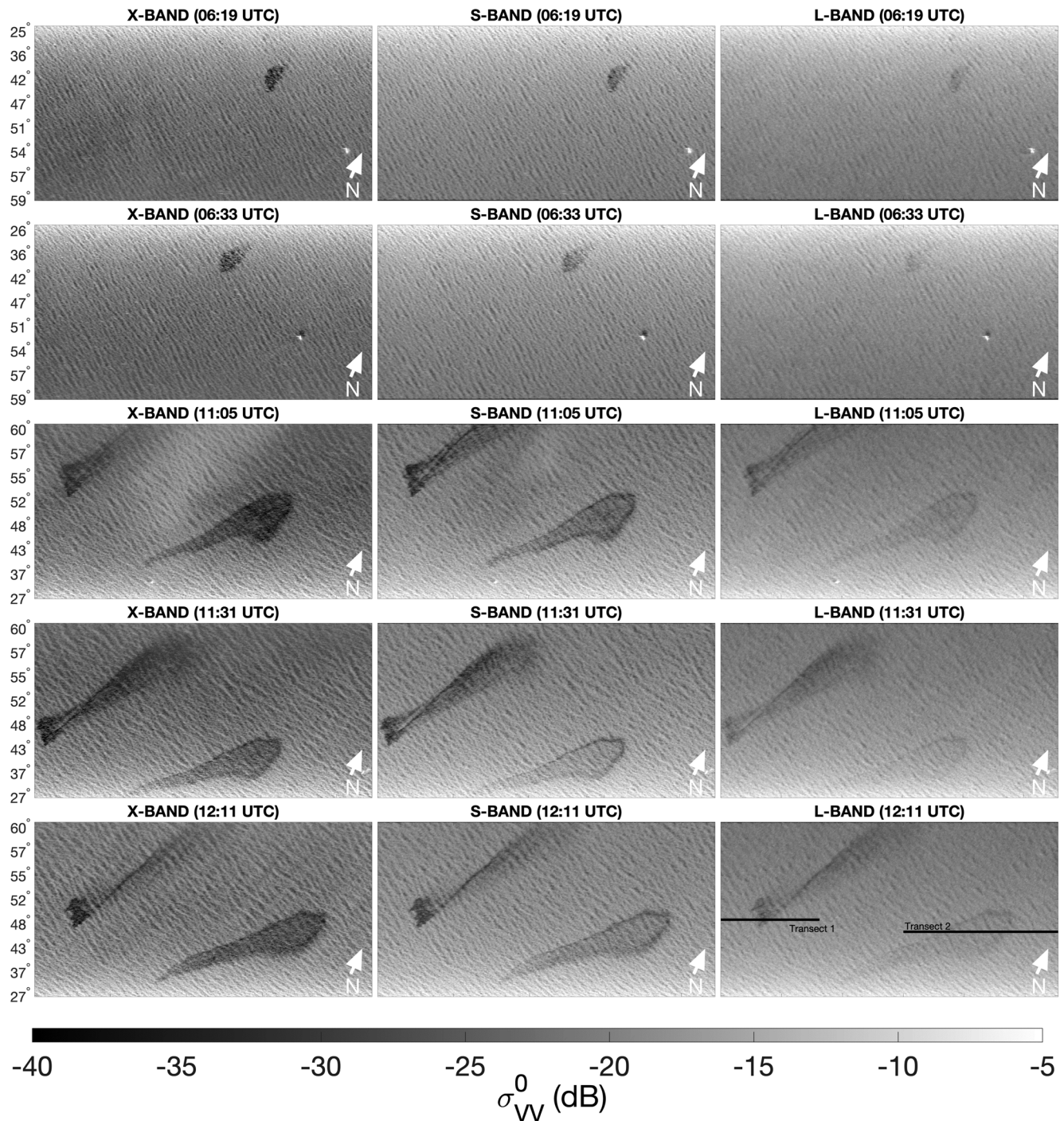


Figure 8. Time series of F-SAR images acquired simultaneously with the X- (left), S- (center), and L-band (right) instruments. Within all the images, the topmost oil slicks are mineral oil, whereas the bottom-most slicks are soybean oil. The first row contains only the mineral oil slick. The soybean oil release is initiated in the second row, where RV HH is identified as a bright spot. The numbers on the y-axis (range direction) represent the incidence angle, and the azimuth direction is along the x-axis. The locations of two transects along the azimuth (Figure 9) are shown in the lower right panel. The images are shown in radar coordinates. Abbreviation: RV HH, research vessel Helmer Hanssen.

angle, and this algorithm automatically determines the number of classes (segments) using a goodness-of-fit test that is sequentially applied around the EM stage. The output of this algorithm is a collection of unlabeled classes, and we therefore need to identify and select the classes representing oil and clean sea. The class (only one class) representing the lowest VV-backscatter within the oil slick is selected as thick oil.

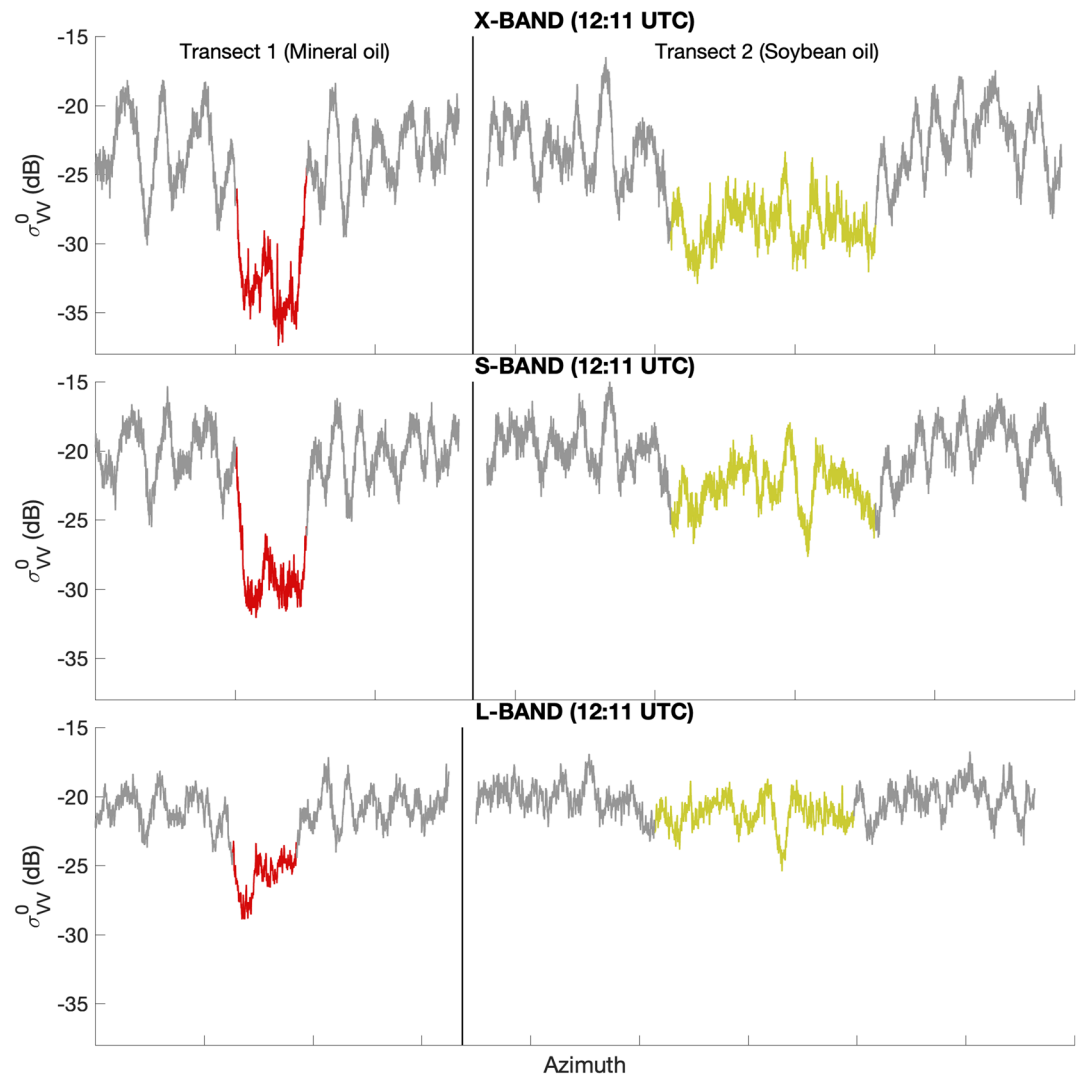


Figure 9. VV-intensities (σ_{VV}^0) from the two transects covering mineral oil (red) and soybean oil (green) indicated in Figure 8. The profiles are averaged over a line width of 50 pixels in the range direction. Transect 1 has 13,000 pixels for X- and S-and, and 6,500 pixels for L-band along azimuth. Transect 2 has 20,536 pixels for X- and S-and, and 10,268 pixels for L-band along azimuth.

Therefore, we assume that the lowest backscatter, that is, highest oil-sea contrast, represents the thickest oil. As a consequence of the high wind, this algorithm struggled to cleanly segment the entire slick from both the mineral and soybean oil, and the darker wave bottoms were segmented into several of the same classes as the oil slick, making it challenging to obtain a pure oil slick mask. Therefore, rather than trying to find different scaling and tuning to improve the separation, the entire oil slick masks were drawn manually.

Figure 10 shows the manually segmented slick masks of the soybean and mineral oil (yellow and black), and the semi-automated thick oil masks (red). All the slick masks are from the F-SAR time series. The four mineral oil masks from the left in Figure 10 are from flight 1 (see Table 3), and are taken close after the mineral oil release. The following oil masks are derived from flight 2, and are larger in size and elongated in shape. The small-sized mineral oil masks in the last part of this sequence is a result of the slick being cropped as it is located on the edge of the scene at a high incidence angle. The leftmost soybean oil mask covers the oil when it was undergoing release. From the F-SAR time series of slick masks laid out in Figure 10 and the calculated area in Figure 11, the development of oil spill spread-out with time is evident. Additionally, the majority of the oil masks are similar in shape and size between the soybean and mineral

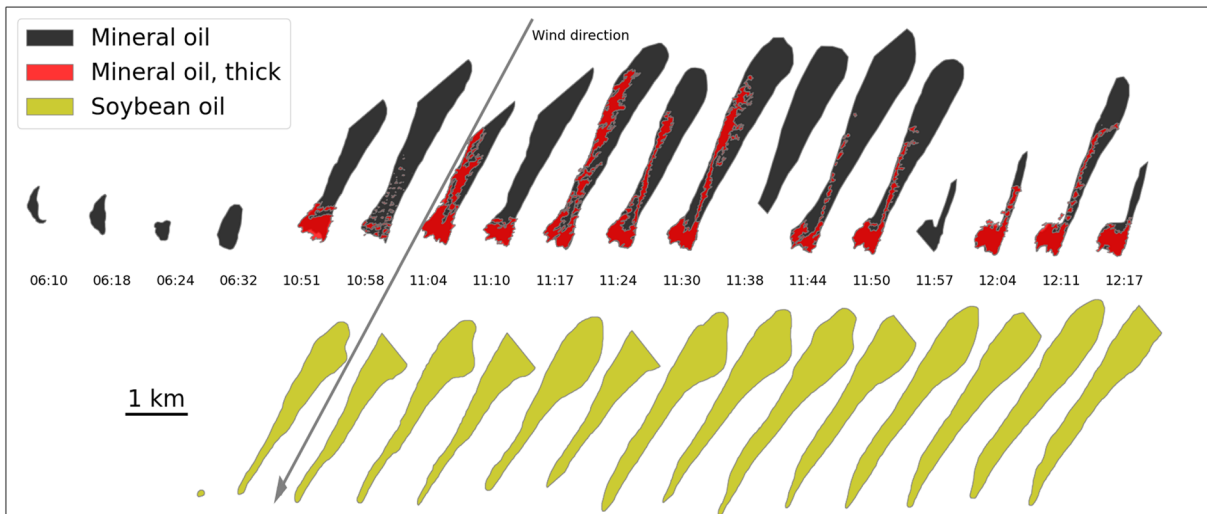


Figure 10. Time series of the oil masks as detected from the F-SAR using the S-band scenes. The upper row shows the mineral oil slick (black), where the thicker parts (semi-automatically segmented) are indicated in red. The lower row shows the soybean oil areas at the same times (UTC), except for the three first times which were before its release. The gray arrow indicates the average wind direction (from 28° clockwise from North) as measured from the SailBuoy between the release and 12:00UTC. North is on top, in this figure.

oil with an elongated shape and wide end. The downwind (southwest) part of the mineral slick has a wide “head” with a diameter of about 500 m, probably consisting of oil that has not been entrained. The soybean oil has a much narrower head, of about 100 m, indicating that the soybean oil did not spread equally much laterally in the crosswind direction.

4. OpenOil Drift Model

To simulate the drift of oil, we have used the open-source oil drift model OpenOil (Röhrs et al., 2018), which is implemented within the generic OpenDrift framework (Dagestad et al., 2018). The horizontal drift is calculated as the vector sum of ocean currents and Stokes drift due to surface gravity waves. An additional wind drift component of 2% of the wind speed at 10 m (e.g., Jones et al., 2016) has to be added to the velocity at the surface, to compensate for the fact that typical ocean models do not resolve the very strong shear observed

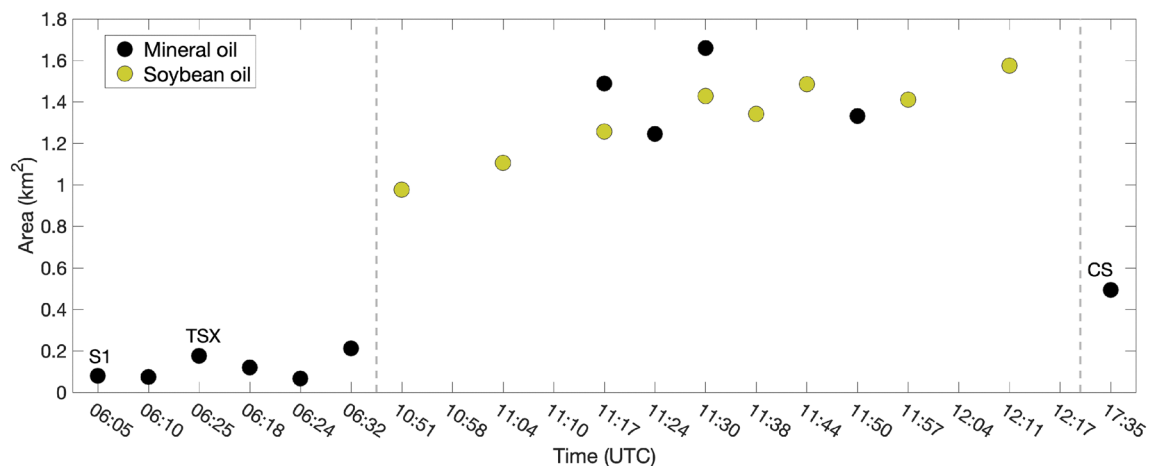


Figure 11. Change in oil slick area versus time. The black and green markers represent the mineral and soybean oil slick from F-SAR (using the S-band scenes) unless specified as one of the spaceborne satellites Sentinel-1, TerraSAR-X, or Cosmo SkyMed. The slick area is only extracted from F-SAR scenes that cover the entire slick. Hence, some markers at given times are missing.

in the upper few decimeters of the ocean (Laxague et al., 2018; van der Mheen et al., 2020). The same is necessary when retrieving the surface current from a near-surface drifter, as described in Section 2.2. Together with the Stokes drift (typically 1.5% of the wind at the surface), this wind drift combines to about 3.5% of the wind speed, as found by several empirical studies (Röhrs & Christensen, 2015; Schwartzberg, 1971).

As the vertical shear of horizontal velocity is very strong near the surface, it is essential to accurately describe the vertical motion and distribution of oil droplets. This involves the entrainment of surface oil due to breaking waves, size spectra, and buoyancy of the entrained oil droplets, and vertical turbulent mixing. These mechanisms and their implementation in OpenOil are described in detail in Röhrs et al. (2018). In this study, we will look at the entrainment of oil from the surface slick into the water column, which is shown to play a role in explaining the development of this surface slick. From Equations 1–3 in Röhrs et al. (2018), as based on Li et al. (2017), the entrainment rate Q is determined by the wave height H_s , wave period T_p and wind speed U_{10m} as follows:

$$Q \propto H_s^{1.805} F_{bw} \quad (2)$$

where F_{bw} is the fraction of the sea surface covered by breaking waves per unit time, as given by Holthuijsen and Herbers (1986):

$$F_{bw} = \begin{cases} c_b \cdot \frac{U_{10m} - U_0}{T_p} & \text{if } U_{10m} > U_0, \\ 0 & \text{otherwise,} \end{cases} \quad (3)$$

where $c_b = 0.032$ s/m is a constant, U_{10m} is the wind speed at 10 m above the sea surface, $U_0 = 5$ m/s, and T_p is the peak (or significant) wave period. Equation 3 implies that entrainment of oil droplets begins at wind speeds of 5 m/s, though some studies have indicated that the threshold should be at a lower wind speed, as discussed in Li et al. (2017). The amount of entrained oil then depends on the wind speed and wave characteristics, and furthermore on the oil type and degree of emulsification, where a higher water content implies higher viscosity and less entrainment (Equations 1–5 in Röhrs et al., 2018).

The probability, p , for a numerical surface particle to be entrained during a simulation time step Δt is given as

$$p = 1 - e^{-Q\Delta t}. \quad (4)$$

The OpenDrift framework provides flexibility using various forcing data, such as wind, waves, and currents. Most commonly, environmental conditions from ocean and atmospheric circulation and wave models are used in oil spill simulations. However, in this study, we also use wind from the SailBuoy and currents retrieved from the CODE drifter that was released together with the mineral oil, using the method described in Section 2.2.

For oil weathering calculations, OpenOil is coupled to the Python version of the ADIOS oil library and database, as developed by NOAA (<https://github.com/NOAA-ORR-ERD/OilLibrary>). However, the database which consists of more than 1,000 different oils does not contain soybean oil, and it is also not possible to model mixtures. However, the oils are already pre-evaporated and emulsified before the release, and thus it is reasonable to assume that the densities and viscosities (Table 1) are kept constant during the simulations. Therefore, evaporation and emulsification processes are disabled during the simulations.

5. Simulated and Observed Oil Slick Drift

Next, we compare various oil drift simulations with the observational time series, consisting of remote sensing imagery (radar and optical data from air and space), the ship's position while collecting thickness samples of the mineral slick, and in situ measurements (drifter measurements at different depths). The main comparison is performed between the oil drift simulations and the oil masks derived from the S-band

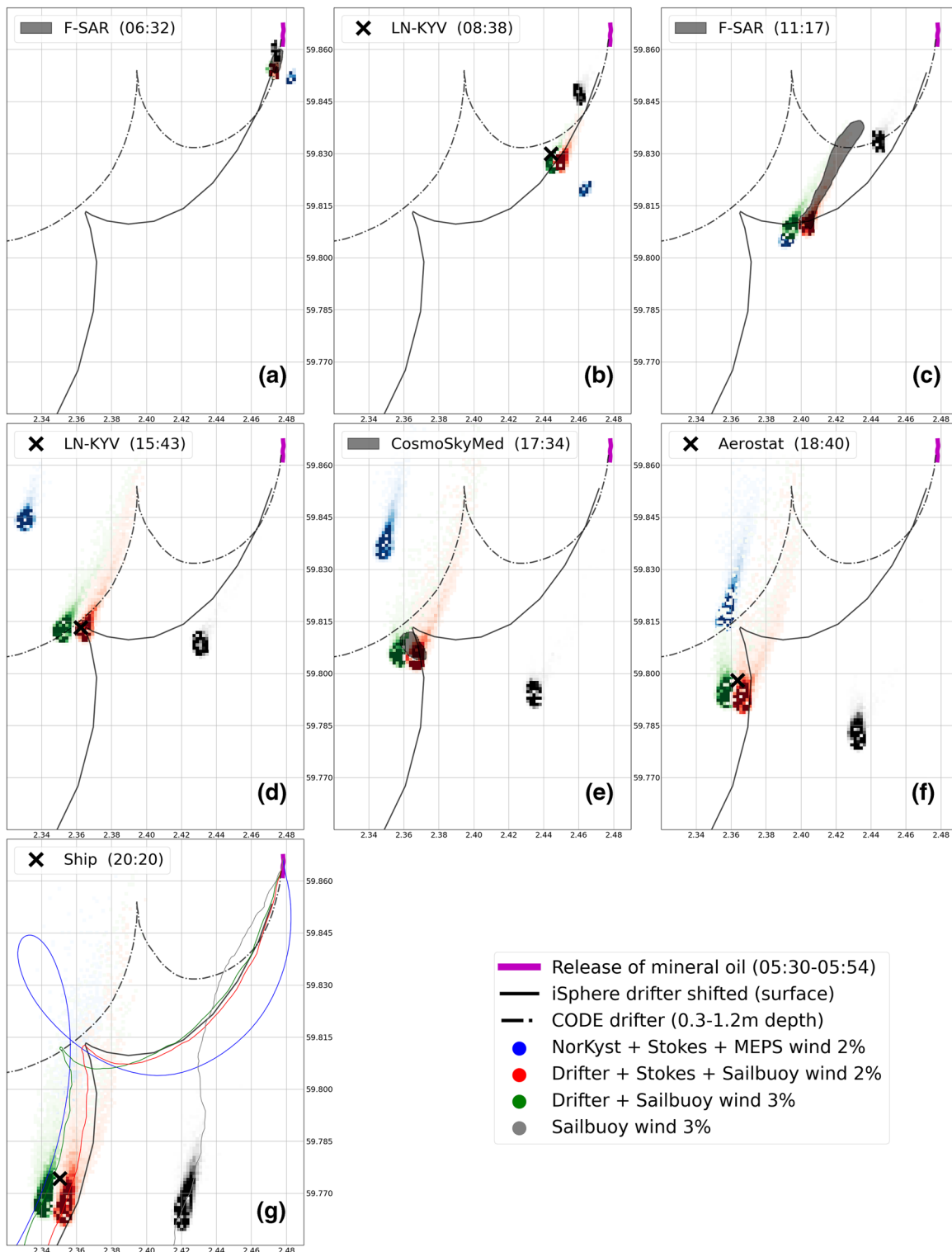


Figure 12. Location of simulated oil slicks at seven different times ((a) - (g)), corresponding to selected observations as indicated in the legends. The solid black line shows the shifted trajectory of the iSphere drifter (see text for explanation), and the dashed black line shows the trajectory of the CODE drifter. The colors of the simulated oil slicks correspond to simulations (see text for details) with four different sets of forcing. Blue: currents from the ocean model, Stokes drift from the wave model, plus 2% of the wind as obtained from the atmospheric forecast model (see Table A1). Red: the same as blue, except that the current is retrieved from the CODE drifter (dashed line, see text for details), and the wind is retrieved from the SailBuoy measurements. Green: the same as red, but omitting the Stokes drift and using instead a higher wind drift factor of 3%. Gray: using only wind (3%) to calculate the drift. In the last figure (lower left), the trajectories of the centroid of the corresponding slicks are shown in the same colors.

F-SAR scenes. We discuss the simulation of the trajectory of the mineral oil slick only; however, these simulations should also be representative of the soybean oil slick, as both the viscosities (Table 1) and observed drift (Figure 4) are nearly the same as for the mineral oil.

In Figure 12, we compare the simulated oil slicks with seven observed masks and positions at different times, from satellite, aircraft, aerostat, and ship, all aligned along the shifted iSphere trajectory.

Four different simulations are shown in different colors, using four corresponding sets of wind, waves, and currents. The absolute distance between the geometrical mean positions of the simulated and observed oil slicks is shown in Figure 13, using the same colors, where all the observed locations of Figure 4 are used.

In Figure 12, the simulation shown as red colors and lines are using the best possible forcing data available for this case study: near-surface currents as retrieved from the CODE drifter, winds from the SailBuoy, and Stokes drift from the wave forecast model. The background currents based on the CODE drifter are here assumed to be constant throughout the water column. The agreement with the observed drift, which is also closely aligned with the shifted iSphere drifter, is seen to be near-perfect, confirming the drift parameterizations as described in Section 4.

The simulated oil slick also nicely reproduces the extent and distribution of oil within the slick, as seen most clearly in the snapshot at 12:11UTC presented in Figure 14. Most of the oil is confined to an area of about 500 m radius at the front, which is also the only part which is observed by all satellites and airborne sensors, except for the F-SAR. The tail of thinner oil as only observed by the F-SAR is nicely reproduced in the simulation, and is aligned almost exactly with the wind directions behind the thicker area at the front (southwest). The leftmost part of Figure 14 shows each of the simulated oil particles, overlaid on the F-SAR observations. Yellow particles are submerged, whereas red particles are at the surface, and only these should correspond to the surface observations. The red particles confined to the tail are lagging behind the main slick as they have been entrained at an earlier time, thus advected at a slower speed (no windage and little Stokes drift), until eventually being resurfaced. As seen in Figure 15, only about 3% of the oil is submerged at the time of Figure 14 (12:11UTC), whereas about 30% of the oil has been entrained at an earlier time. From the oil at the surface, a film thickness is calculated (also shown in Figure 14) by summing the oil mass within bins of 50 m × 50 m, and assuming that the oil is evenly distributed. A thickness of up to 250 μm is observed in the thickest part in the front. As it is observed in situ that the oil thickness is rather heterogeneous and patchy, this calculated thickness should be lower than the thickness in the thickest parts. For most

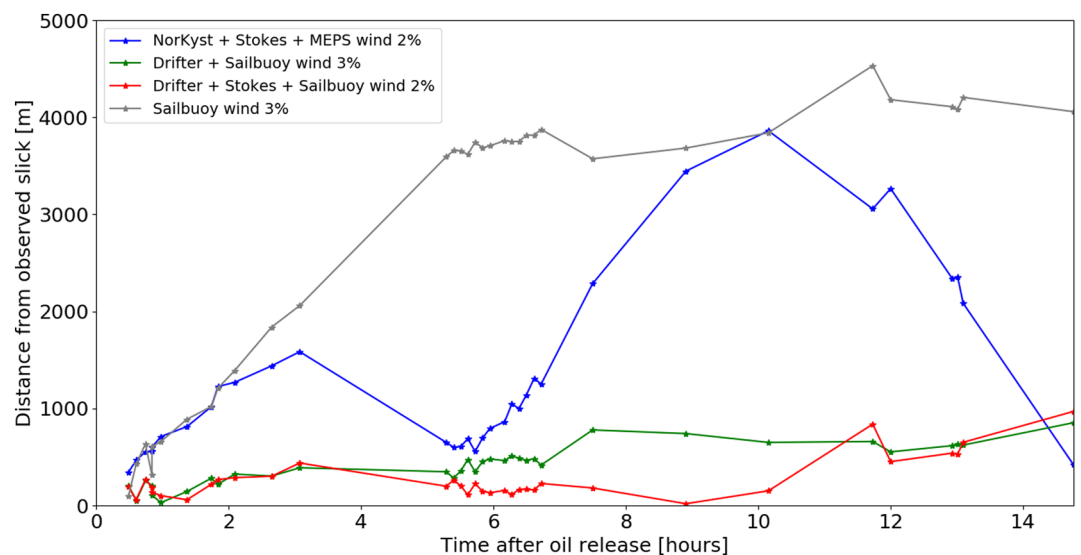


Figure 13. Spatial distance (m) between the geometrical center of the simulated oil and the corresponding observations, as shown in Figure 4. For the oil masks derived from the S-band F-SAR observations, as shown in Figure 10, the centroid is calculated from only the downwind (southwestern) part of the slick, where the oil mass center is located (estimated manually).

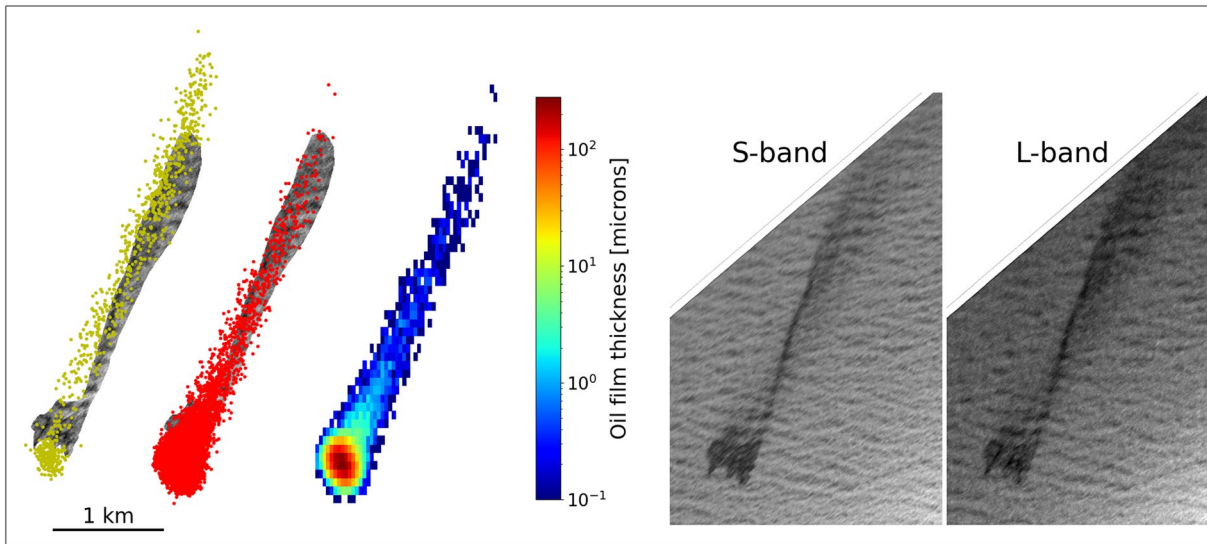


Figure 14. A detailed zoom comparing the simulated oil slick location and extent with F-SAR imagery at 12:11UTC. To the left are simulated oil particles which are submerged (yellow) and at the surface (red) overlaid on the oil mask extracted from F-SAR. More to the right is surface oil film thickness (with colorbar) calculated by averaging surface oil amount in bins of 50×50 m and assuming the oil is uniformly distributed. On the right, the oil slick as observed by F-SAR S-band and L-band is depicted, respectively.

of the tail, the calculated thickness is less than $1 \mu\text{m}$, which is reasonable given that this tail is barely visible by eye and on spaceborne SAR images. It should be noted that the extent and internal variations within the oil slick mainly depend on the wind speed and the oil properties (viscosity). Thus, these internal variations are very similar for all the simulations using different sets of forcing data, although the overall trajectory of

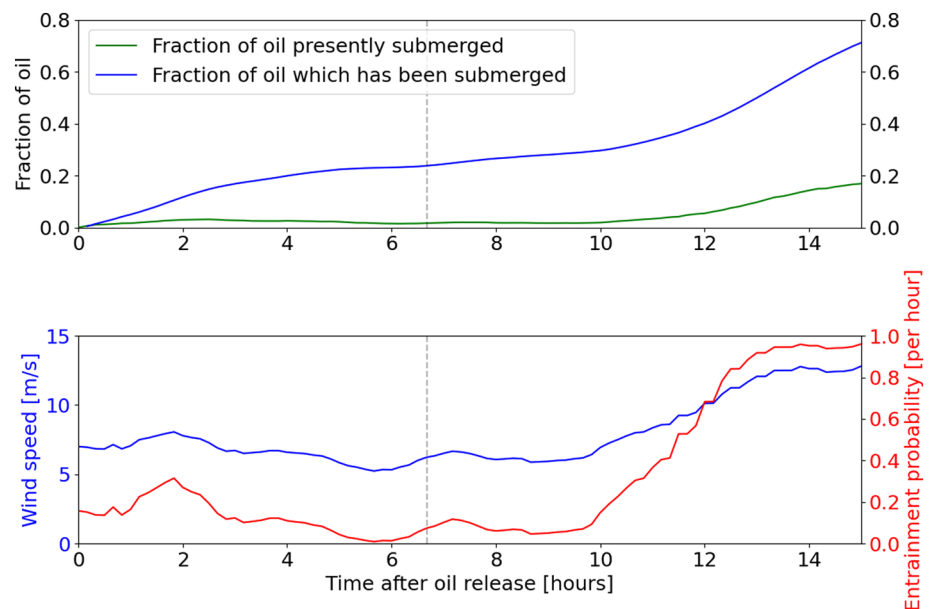


Figure 15. Top: Fraction of the oil which is submerged versus hours since the start of simulation (05:30UTC), for the simulation using in situ measurements for wind and currents (red colors in Figure 12). Green lines show the fraction of oil submerged at the given time, and the blue line shows the fraction of oil which has been submerged, but possibly resurfacing. Bottom: Hourly entrainment probability according to Equation 4 (red) together with the windspeed from the SailBuoy (blue). The vertical line indicates the time of the masks as shown in Figure 14 (12:11UTC).

the oil is rather different, and highly dependent on the ocean currents, as seen in Figure 12. A more in-depth analysis and measurements of the oil budget will be done in a future study.

The simulation shown in blue colors in Figure 12 is based on the operational forecast models for current, wind, and waves (Table A1). This is the same simulation setup as would be used by the operational contingency system at MET Norway, for the normal situation where no in situ measurements are available to assist the prediction. The full trajectory for this simulation, as shown as the blue line in the bottom panel (g), follows an oscillatory path with the same phase as the observations, however, with a larger amplitude. At this latitude (60N), the inertial cycle is about 13.8 h. Thus, although this simulated trajectory deviates a bit from the observed trajectory, it coincides almost perfectly with the observed oil slick location at around 20:20UTC, about one inertial period after the oil release. This implies that the direct wind-induced drift and background currents here agree with each other, but that the error in the amplitude of the inertial oscillation causes poor predictability at forecast lengths different than an integer repetition of the inertial cycle during this particular case study.

Such inertial oscillations are a dominating feature of the ocean circulation in this region, as also observed by Jones et al. (2016) and Christensen et al. (2018). Overestimation of the inertial oscillation amplitude in the ocean model can be caused by too shallow or too strong stratification, too weak mixing, or too large wind speeds in the atmosphere model (Röhrs & Christensen, 2015). It is positive to notice, however, that the existence and phase of the inertial oscillation in the model are captured well in this case.

Two more simulations are shown in Figures 12 and 13, respectively. Green colors represent a simulation using currents from the CODE drifter, but using a wind drift of 3%, instead of 2% wind drift and additional Stokes drift. The near-perfect alignment with the observations indicate that the Stokes drift in this case is well parameterized as 1% of the wind, in fair agreement with Ardhuin et al. (2009). It should be noted that the simulated (as well as the observed) oil may have spent some of the time entrained below the surface, thus temporarily subject to a lower Stokes drift than at the surface.

A last simulation is shown in gray color, using simply 3% of the wind as the horizontal forcing, with no current and Stokes drift. This simulation yields the lowest accuracy, and does not include the dominating inertial oscillations. The overall direction of propagation fits within about 30° of the observed drift. It is interesting to note that applying the old rule of thumb that “drift is 30 degrees to the right of the wind” would have provided a fairly accurate estimate of the oil location after one inertial period (not shown). This rule of thumb has observational support by Ardhuin et al. (2009), who found that measured surface currents are on average (with tides filtered) between 10° and 40° to the right of the wind (Northern Hemisphere).

The simulated masks shown in the figures include only the surface part of the oil, as do the observations; however, the extent of the tail is anyway a result of the combined horizontal and vertical transport. The amount of oil entrained at any time during the simulation is shown in Figure 15, upper panel. The lower panel of the same figure shows the concurrent hourly entrainment probability (Equation 4), along with the observed wind speed. During the first 10 h of the simulation, less than 3%–4% of the oil is submerged at any time, although the hourly entrainment rate is above 20% in the first few hours. This indicates that most of the entrained oil is fairly quickly resurfacing. After about 10 h, an increase in the wind speed from about 7 to 10 m/s gives a proportionally larger increase in the entrainment probability and submerged fraction. This is consistent with Equation 3 which predicts that there is no whitecapping with wave entrainment before the wind speed exceeds 5 m/s.

6. Mineral Oil Slick Characteristics in SAR Versus Optical Imagery

This section addresses the similarities and dissimilarities between the SAR (F-SAR) and optical (LN-KYV) acquisitions in detection of the slicks. The F-SAR flight #1 time series covers 1–2 h after the mineral oil release, whereas the second flight (F-SAR flight #2) covers ~6–7 h after the release (see Figure 2). LN-KYV was also flying before and after the F-SAR flights collecting both visible (RGB parts of the electromagnetic spectrum) and IR videos. The combined use of the SAR and optical (RGB and IR) images result in a unique time series with high temporal sampling of the oil spills. The scenes that are closest in time (less

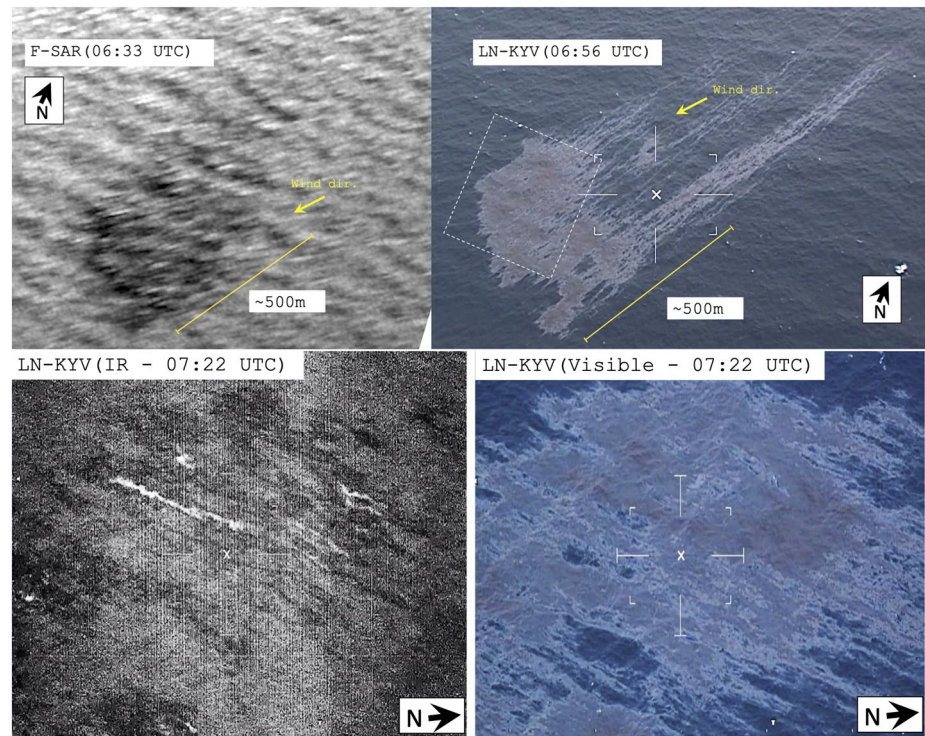


Figure 16. Top: Imagery from F-SAR flight #1 and LN-KYV flight #1. The F-SAR S-band image was acquired 06:33UTC. Bottom: overlapping zoomed-in IR and visible images taken at 07:22UTC from the white dashed square (approximate location) in the top-right image, and covers the same area of the slick taken at the exact same time (images published with permission from NOFO). IR, infrared; NOFO, Norwegian Clean Seas Association for Operating Companies.

than 1 h) between the F-SAR and LN-KYV (both visible and IR) are discussed in this section, and only a selection of snapshots from the RGB/IR videos are shown. The crew onboard the DLR aircraft with the F-SAR instrument took photographs of the slick, which are also discussed. The image material is displayed in Figures 16–18.

In the top panel of Figure 16, a close in time SAR scene from F-SAR and an optical scene from LN-KYV are shown. These scenes are acquired ~30 min to an hour after the release of the mineral oil emulsion. The shape and size of the oil patch are similar in the optical and F-SAR images, and a wider oil front is observed followed by a thinner tale behind it. The white areas (IR-white) in the IR image of Figure 16 reveal the presence of relatively thick oil of $>50 \mu\text{m}$, which is classified as true color according to the BAOAC (Bonn Agreement, 2016; Fingas & Brown, 2014). This is because thick oil appears “heated” compared with the surrounding water in infrared images (Fingas & Brown, 2014). The dark patches in the IR image might correspond to intermediate thick oil layers that appear “cool” using IR. True color can also be seen in the visible image, where dark brown colored patches can be observed, as well as metallic/sheen. These observations were also noted by a trained pilot onboard LN-KYV on both the flights (Figures 16 and 17).

Three oil patches can be seen in the optical image (LN-KYV) in Figure 17 and in the right photo of Figure 18. Thick oil is often surrounded by sheen (unless the oil is heavily weathered) (Leifer et al., 2012). In the right panels of Figures 17 and 18 the oil types that are most likely present are thick oil (true color) surrounded by sheen/metallic. The three patches can also be seen in the F-SAR image, but there they are connected to each other, which is most likely a result of different imaging techniques (optical vs. microwaves). Note that the right photo of Figure 18 was taken 8 min prior to the F-SAR image, and in the photo the oil has a similar shape and structure as in the photo from LN-KYV (1 h after).

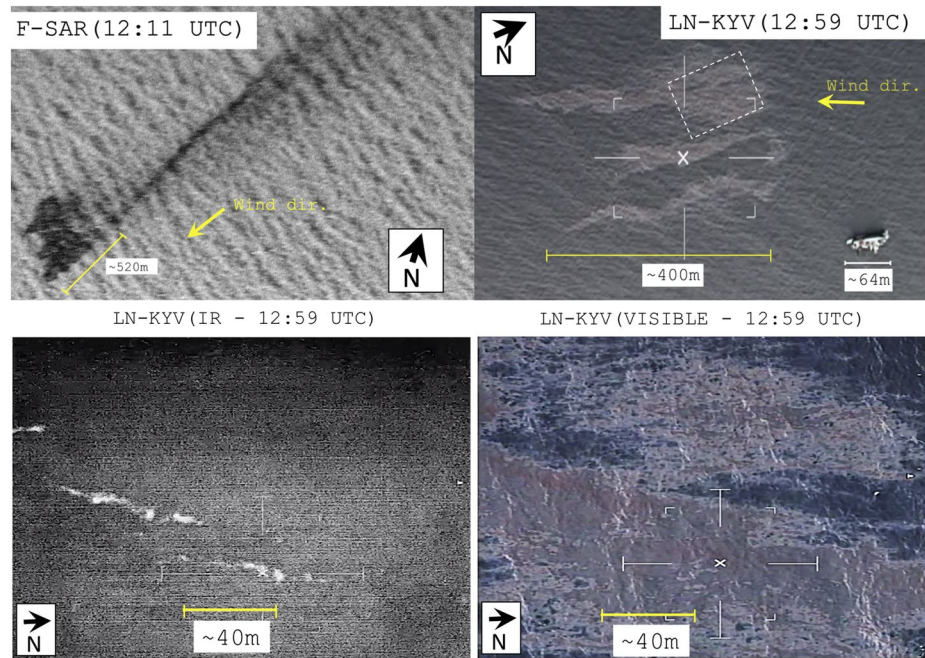


Figure 17. Top: Imagery from F-SAR flight #2 and LN-KYV flight #2. The F-SAR S-band image was acquired 12:11UTC. Optical (RGB) from LN-KYV covering the mineral oil slicks at 12:59UTC. Bottom: overlapping zoomed-in IR and visible images from the white dashed square (approximate location) in the top-right image, and the IR and RGB images cover the same area taken at the exact same time (images published with permission from NOFO). IR, infrared; NOFO, Norwegian Clean Seas Association for Operating Company; RGB, red, green, and blue.

Internal variations, indicating surface layers of different oil thickness, are also observed between the main patch (with the three “spikes”) and the elongated slick trailing the main patch in the F-SAR image. This tail is not visible in the optical scene in Figure 17. However, a trace of this tail can be observed in the photograph taken during the F-SAR flight (see left photo of Figure 18). The elongated slick is present in the optical image acquired 06:56UTC (see Figure 16), but not in the optical image acquired 12:59UTC in LN-KYV flight #2. The elongated slick is not detected in any of the videos/images from LN-KYV flight #2, even though the airplane flew around the slick resulting in different viewing angles. According to the left photo in Figure 18, this tail can be spotted at steeper viewing angles. The oil-sea contrast depends on the viewing angles (zenith and azimuth angles) as well as the Sun’s zenith and azimuth angles (Otremba & Piskozub, 2004; Sun & Hu, 2019), which explains the different oil-sea contrast between the visible images in Figures 17 and 18. At this point, the oil has spread, weathered, and oil droplets have also been vertically mixed into the water column. The main oil patch seen in the visible and F-SAR images have a similar size (500 m). In conclusion,

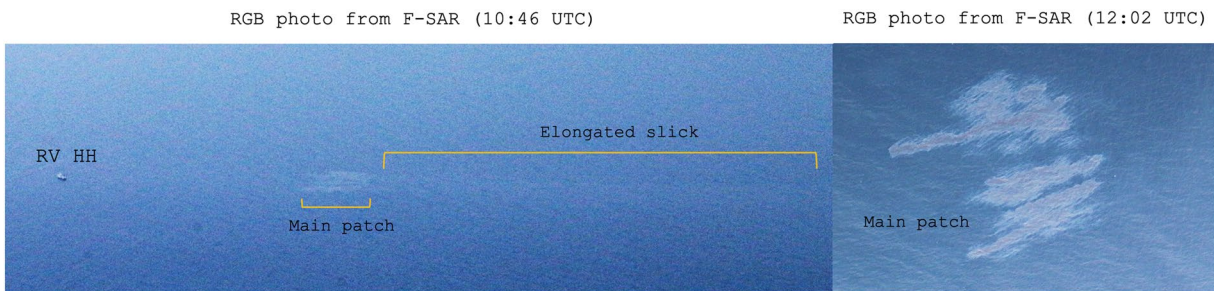


Figure 18. Photos from F-SAR flight #2 taken by Ralf Horn at DLR. The left image was acquired at the beginning of flight #2, whereas the right image was taken at the end. Both images have been contrast enhanced (photos published with permission from NOFO). DLR, Deutsches Zentrum für Luft-und Raumfahrt; NOFO, Norwegian Clean Seas Association for Operating Company.

some parts of the oil might be invisible in the optical region, but are clearly visible in the microwave region. The lower panels of Figure 17 show overlapping zoomed-in IR and visible images (from the dashed white box) taken at the same time from LN-KYV. Observations of IR-white patches can again be seen, and these correspond to the very dark brown patches in the visible image, indicating thick oil. Note that the IR reflection changes with oil thickness and also with the oil-to-water emulsion rate (Leifer et al., 2012). The oil around the IR-white patches is not detected in the IR image, which is most likely due to the slick being too thin (Leifer et al., 2012), given its sheen/metallic appearance in the zoomed-in visible image. The same internal variations within the main patch are challenging to confirm in the F-SAR image as the optical images cannot be geocoded for direct comparison.

7. Conclusion and Outlook

We have presented an extensive set of measurements in relation to the controlled release of two oil slicks in the North Sea in June 2019. The two surface releases each of 2 m³ consisted of, respectively, a mineral oil emulsion and a soybean oil emulsion. The overall drift of the slicks was very similar, due to similar viscosity. The thickest part of the mineral oil slick followed very closely the track of an iSphere surface drifter. Behind this followed a long tail (4–5 km) of thinner oil. This tail was observed clearly in the airborne SAR data (F-SAR), but is barely visible on airborne and in situ RGB images or by the naked eye. The orientation of the tail was perfectly aligned with the measured wind direction, although the overall drift of the slicks had an additional circular motion due to inertial currents in the ocean.

The drift and evolution of the oil slicks were simulated with the open-source oil drift model OpenOil, from the release starting 05:30UTC on the morning of June 12 until the last recorded observations of the slick position at 20:20UTC the same evening. Good agreement with the observations of both the position and extent of the mineral oil slicks was obtained when using the best possible forcing available, namely, ocean currents as retrieved from a near-surface drifter (CODE), Stokes drift from a wave forecast model, and additional 2% of the in situ measured wind for oil at the surface. It should be noted that these simulations are based on various physical parameterizations as found in the scientific literature, and without using any tuning constants for this specific case.

The extent and tail of the mineral oil slick were accurately resolved by the model, owing to realistic parameterization of the wave entrainment, oil droplet spectra, vertical turbulent mixing, and resurfacing. The single most important physical oil property for the simulations is the viscosity, and in this case the simulations benefited from using measured/known values of the viscosities. In practice, this is often a major uncertainty for the simulations, as both the type of oil, and its degree of emulsification may be poorly known. As the two oils had very similar measured viscosities, the simulated drift and extent of the two slicks were also very similar (but only the simulation for mineral oil is shown in this paper). Additionally, the extent was very similar between the two oils using the manually derived mask from the S-band F-SAR time series. However, the appearance in the optical images and the F-SAR time series were different between the soybean and mineral oil. Furthermore, seabirds were only influencing the soybean oil slick, thus there are different wildlife interactions between the two oils. From a drifting perspective, the biological oil emulsions could replace the mineral oil emulsion for future oil spill preparedness campaigns, as long as the viscosity is similar, and as long as the emulsion is stable, which was apparently the case in this study. However, from a remote sensing and wildlife perspective, the two oils have different properties. Further investigation on how the soybean oil impacted the seabirds must be conducted in order to recommend the soybean oil as a substitute for mineral oil.

In addition to simulations based on in situ forcing data, the oil spill model has also been run with numerical forecast data yielding fair but lower accuracy. Deviation from observed drift arises because the ocean circulation model did not resolve the amplitude of inertial currents accurately that resulted in cycloid motions. However, after one inertial period (13.8 h), this error vanished. Although this conclusion is drawn from one case study only, we expect that for any oceanic drift forecast during the presence of inertial oscillations, the predictability should be relatively higher after integer multiples of the local inertial period, because pure inertial oscillations do not add lateral dispersion (Beron-Vera & LaCasce, 2016). Accurate description of turbulent mixing determining the amplitude of inertial oscillations in ocean models is therefore essential

for drift modeling on timescales of hours to days (Christensen et al., 2018; Röhrs & Christensen, 2015). It should also be noted that inertial oscillations are not visible on maps of currents from models or remote sensing, but these motions dominate drift trajectories in many applications when looking at time series or trajectories. As simulations based on currents retrieved from nearby drifters are found to be more accurate, we recommend deployment of surface drifters near real oil spills, whenever possible. This would, however, require that the data are also made available in near-real time for the modeling. The usefulness may, however, be limited in regions with large spatial gradients of currents, as the drifters may not be representative for currents over the relevant area.

Oil spill simulations using the rule-of-thumb parameterizations for surface drift, that is, assuming the drift is 3% of the wind speed, yielded poorer agreement. Applying an additional directional deviation (30% to the right of the wind), improves the result, at least after one full inertial period. Our carefully controlled experiment and measurements confirm previous indications that the drift of oil at the ocean surface is well parameterized by the sum of ocean currents, Stokes drift, and 2% of the wind. Some elongated wind-aligned linear structures within the slick (see Figure 14), believed to be due to Langmuir circulation, are not reproduced by the simulations. Thus, whereas including parameterizations of Langmuir circulations in oil drift models may possibly add more fine scale variability, this is apparently not important for the overall drift on scales larger than the Langmuir cells themselves (meters to kilometers).

Our findings reveal differences in detection capabilities of the thinnest regions within the mineral oil slick between the F-SAR and optical images, indicating that SAR detects a larger extent than optical imagery. Both sensors detected the thickest part of the oil, but the thinnest parts were observed using the F-SAR sensor only. F-SAR detects the very thin tail, showing superior detection compared with other measurements. However, this thin part (“sheen”) is normally irrelevant to cleaning operations, which have to focus on the thicker (“collectable”) parts. Thus, the high detectability might in fact be a problem, unless one also has an indication that the thickness is very low. The highest oil-sea contrast was found using X- and S-bands compared with the L-band. It is also possible to observe differences between the thickest and the thinnest parts of the oil using F-SAR, but this should be further investigated using the damping ratio combined with the optical images. We also discovered that the soybean and mineral oils were different by evaluating the visual appearance between the two oils in both the F-SAR and optical images. For the mineral oil, a clear internal variation between the tail and the main patch could be observed indicating different thicknesses, while for the soybean oil a homogeneous film was observed with an outer rim. The extent and drift were similar between the two oils.

Although this experiment was well organized with a successful collection of various types of data, some improvements and recommendation can be made. For example, one of the objectives of this study was to find a greener substitute for mineral oil, and the soybean oil emulsion was tested. As already mentioned, if the goal is to evaluate the overall drift behavior, then the soybean oil could be used as a substitute for future oil spill exercises, as long as the oil volume is kept to a minimum, since a huge amount of soybean oil has been reported to harm wildlife (Rigger, 1997). In the chase for a greener substitute to mineral oil, that has the same drifting and spreading behaviors, little impact on wildlife, and/or appearances in optical and SAR imagery, various alternative substances should be tested in future exercises. Another objective of this study was to compare the SAR and optical data. Unfortunately, this comparison is somewhat limited, since the optical data could not be properly geocoded, which is, however, possible for the F-SAR scenes. In future campaigns, the systems acquiring the optical data should also collect enough auxiliary information for geocoding purposes. The SAR instrument is a powerful tool for oil spill monitoring due to its independence of the Sun and weather conditions, whereas optical sensors are limited by light and cloud conditions. In the past decade, studies have demonstrated that SAR images of oil slicks are not limited to only detection, but have a potential for characterizing the oil slicks in terms of locating relative thicker and thinner oil patches, which this study supports. Based on this study, we recommend to prioritize SAR on aircraft for recovery and preparedness of oil spill operations, where optical data could act as a complementary data source for validation of what we observe in the SAR scenes.

As a future work, we plan to look closer into the oil budget and vertical entrainment of oil droplets during this experiment. The potential of multifrequency SAR oil spill characterization will also be investigated in more depth by utilizing the F-SAR data collected in this experiment.

Appendix A: Operational Forecast Models

Operational forecast models used for drift simulations in this study are presented in Table A1.

Table A1

Operational Forecast Models of MET Norway, which are Used for the Drift Simulations of This Study

Model	Variables	Resolution
NorKyst (ROMS)	Currents, temperature, salinity	800 m
MyWaveWAM (WAM)	Waves, Stokes drift	4 km
MEPS (Arome)	Wind, air temperature	2.5 km

Note. NorKyst800 m is a coastal setup of the ROMS ocean model with 800 m horizontal grid spacing, without data assimilation (free run). It is forced by winds from the MEPS/Arome atmospheric model, which is a non-hydrostatic model run with 2.5 km grid spacing, forced on the boundaries by the global ECMWF model. The ocean currents are provided at the following depths near the surface (in meters): 0, 3, 10, 15, 25, and 50. The MyWaveWAM model is a version of the WAM wave model, also forced by winds from MEPS/Arome and ECMWF, run with 4 km grid spacing. In the text, these are referred to as “forecast models.”

Appendix B: Properties of the SAR instruments

Properties of the airborne and spaceborne SAR sensors utilized in this study are presented in Table B1.

Table B1

Sensor Properties of the F-SAR Instrument (Horn et al., 2009; Reigber et al., 2012), TerraSAR-X (Fritz & Eineder, 2013), Sentinel-1 (Bourbigot et al., 2016), and COSMO-SkyMed-1 (ScanSAR Huge Region mode) (Battagliere & Virelli, 2019; eoPortal Directory, 2020).

SAR instrument	F-SAR			Terra-SAR-X	Sentinel-1	COSMO-SkyMed-1
Freq. band	X	S	L	X	C	X
Wavelength (cm)	3.12	9.22	22.63	3.11	5.55	3.12
Freq. (GHz)	9.6	3.25	1.325	9.65	5.405	9.6
Polarizations	HH, HV, VH, VV			HH, VV	VV, VH	VV
Res. (rg. × az.) (m)	0.2 × 0.2	0.5 × 0.35	1 × 0.4	1.2 × 6.6	20 × 22	100 × 100
Swath width (km)	~3.2	~3.2	~3.2	30	250	200
Incidence ang. (°)	23–60	23–60	23–60	28	29–46	18–60
NESZ (dB)	−34/−45/−30	−29/−48/−41	−47/−58/−55	−22.3 ± 1.4	<−23.7	−21/−22

Note. The F-SAR carries X-, C-, S-, L-, and P-band sensors (Horn et al., 2009; Reigber et al., 2012), but only X-, S-, and L-bands are shown since these were used during NORSE2019. The Noise Equivalent Sigma Zero (NESZ) values are approximate and represent along near-, mid-, and far-ranges. The Sentinel-1 scene is the Interferometric Wide swath mode with the ground range detected product.

Abbreviation: NESZ, Noise Equivalent Sigma Zero.

Data Availability Statement

NorKyst800, MEPS, and MyWaveWAM data are openly available: thredds.met.no. SailBuoy weather measurements: <http://doi.org/10.5281/zenodo.3898556>. MetOcean drifter data: <http://doi.org/10.5281/zenodo.3898521>. Output from oil drift simulations: <http://doi.org/10.5281/zenodo.3901003>. Oil slick masks derived from F-SAR: <https://doi.org/10.18710/YOILRP>.

Acknowledgments

The NORSE2019 campaign was funded by CIRFA through the RCN (grant no. 237906) and partners. Dagestad and Hole were supported in part by a grant from The Gulf of Mexico Research Initiative (#G-231819). The authors sincerely thank NOFO for including the experiment in their exercise. In particular, they thank the crew from NOFO onboard RV HH and Kristin K. Husebye at NOFO HQ for her efforts in accommodating their numerous requests (access to the data from LN-KYV and aerostat used in this study needs to be requested; email: kh@nofo.no). They also thank DLR and the crew onboard the F-SAR aircraft, Dr. Stine Skrunes, KSAT, and in particular, Hugo Isaksen for his devotion to the link between research and innovation. They also thank all the participants and observers onboard RV HH, including representatives from CSIRO, NORCE, Env. Canada, and Water Mapping, LLC. Thanks to the European Space Agency for providing Sentinel-1B data (freely available through <https://scihub.copernicus.eu>), DLR/InfoTerra for TerraSAR-X data (obtained through TerraSAR-X Proposal ID AO MTH3174, access needs to be requested through DLR/InfoTerra), and KSAT and Italian Space Agency for the use of oil masks derived from COSMO-SkyMed data (access needs to be requested by Hugo Isaksen; e-mail: hugo@ksat.no). Thanks to Anthony P. Doulgeris at UiT for the use of his algorithm for segmenting the oil slicks.

References

Alpers, W., Holt, B., & Zeng, K. (2017). Oil spill detection by imaging radars: Challenges and pitfalls. *Remote Sensing of Environment*, 201, 133–147.

Ardhuin, F., Marie, L., Rasche, N., Forget, P., & Roland, A. (2009). Observation and estimation of Lagrangian, Stokes, and Eulerian Currents Induced by Wind and Waves at the sea surface. *Journal of Physical Oceanography*, 39(11), 2820–2838. <https://doi.org/10.1175/2009JPO4169.1>

Battagliere, M. L., & Virelli, M. (2019). *Cosmo-skymed mission and products description (Tech. Rep. Nos. ASI-CSM-PMG-NT-001, Issue 3)*. Italian Space Agency. Retrieved from https://www.asi.it/wp-content/uploads/2019/08/COSMO-SkyMed-Mission-and-Products-Description_rev3-1.pdf

Beron-Vera, F. J., & LaCasce, J. H. (2016). Statistics of Simulated and Observed Pair Separations in the Gulf of Mexico. *Journal of Physical Oceanography*, 46(7), 2183–2199. <https://doi.org/10.1175/JPO-D-15-0127.1>

Bonn Agreement. (2016). *Bonn agreement aerial operations handbook Part III- Guidelines for oil pollution detection, Investigation and post flight analysis/Evaluation for volume estimation (Tech. Rep.)*. Retrieved from <https://www.bonnagreement.org/publications>

Bourbigot, M., Johnsen, H., & Piantanida, R. (2016). *Sentinel-1 product definition (Tech. Rep. Nos. S1-RS-MDA-52-7440, Issue 2/7)*. MPC-S1. Retrieved from <https://sentinel.esa.int/documents/247904/1877131/Sentinel-1-Product-Definition>

Breivik Ø., Janssen, P. A. E. M., & Bidlot, J.-R. (2014). Sept. Approximate Stokes drift profiles in deep water. *Journal of Physical Oceanography*, 44, 2433–2445. <https://doi.org/10.1175/JPO-D-14-0020.1>

Brekke, C., & Jones, C. E. (2020). SAR Oil Spill Imaging, Interpretation and Information Retrieval Techniques. In G. D., Martino, & A., Iodice (Eds.), *Maritime Surveillance with Synthetic Aperture Radar* (pp. 227–267). UK: The Institution of Engineering and Technology (IET). In press. ISBN: 978-1-78561-601-3.

Christensen, K. H., Breivik, Ø., Dagestad, K. F., Røhrs, J., & Ward, B. (2018). Short-term prediction of oceanic drift. *Oceanography*, 31, 59–67. <https://doi.org/10.5670/737oceanog.2018.310>

Cristea, A., van Houtte, J., & Doulgeris, A. P. (2020). Integrating Incidence Angle Dependencies into the Clustering-Based Segmentation of SAR Images. *IEEE Journal of Selected Topics in Applied Earth Observations and Remote Sensing*, 13, 2925–2939

Dagestad, K.-F., Røhrs, J., Breivik, Ø., & Ådlandsvik, B. (2018). OpenDrift v1.0: A generic framework for trajectory modelling. *Geoscientific Model Development*, 11, 1405–1420. <https://doi.org/10.5194/gmd-11-1405-2018>

Davis, R. E. (1985). Drifter observations of coastal surface currents during CODE: The method and descriptive view. *Journal of Geophysical Research*, 90(C3), 4741–4755. <https://doi.org/10.1029/JC090iC03p04741>

Doulgeris, A. P., & Cristea, A. (2018). Incorporating incidence angle variation into SAR image segmentation. *IGARSS 2018 - 2018 IEEE International Geoscience and Remote Sensing Symposium*. 8543–8546. <https://doi.org/10.1109/IGARSS.2018.8519043>

Elliott, A. J. (1986). Shear diffusion and the spread of oil in the surface layers of the North Sea. *Deutsche Hydrografische Zeitschrift*, 39(3), 113–137. <https://doi.org/10.1007/BF02408134>

Engen, F., Taban, I. C., Dolva, H., & Holt, H. S. (2019). *Olje på vann 2019 (Tech. Rep. Nos. 38581, Issue 1)*. NOFO. Retrieved from <https://www.nofo.no/globalassets/nyheteraktuelt/opv2019-rapport.pdf>

eoPortal Directory. (2020). *COSMO-SkyMed Constellation of 4 SAR satellites*. Retrieved from <https://directory.eoportal.org/web/eoportal/satellite-missions/c-missions/cosmo-skymed#foot43/>

Espeseth, M. M., Skrunes, S., Jones, C. E., Brekke, C., Holt, B., & Doulgeris, P. (2017). Analysis of evolving oil spills in full-polarimetric and hybrid-polarity SAR. *IEEE Transactions on Geoscience and Remote Sensing*, 55(7), 4190–4210. <https://doi.org/10.1109/TGRS.2017.2690001>

Fingas, M., & Brown, C. (2014). Review of oil spill remote sensing. *Marine Pollution Bulletin*, 83(1), 9–23. <http://dx.doi.org/10.1016/j.marpolbul.2014.03.059>

Fritz, T., & Eineder, M. (2013). *TerraSAR-X ground segment basic product specification document (doc: TX-GS-DD-3302)*. DLR.

Gade, M., Alpers, W., Hühnerfuss, H., Masuko, H., & Kobayashi, T. (1998). Aug. Imaging of biogenic and anthropogenic ocean surface films by the multifrequency/multipolarization SIR-C/X-SAR. *Journal of Geophysical Research*, 103(C9), 18851–18866.

Ghani, M. H., Hole, L. R., Fer, I., Kourafalou, V. H., Wienders, N., Kang, H., et al., (2014). The SailBuoy remotely-controlled unmanned vessel: Measurements of near surface temperature, salinity and oxygen concentration in the Northern Gulf of Mexico. *Methods in Oceanography*, 10, 104–121.

Hole, L. R., Fer, I., & Peddie, D. (2016). Directional wave measurements using an autonomous vessel. *Ocean Dynamics*, 66(9), 1087–1098.

Holthuijsen, L. H., & Herbers, T. H. C. (1986). Statistics of Breaking Waves Observed as Whitecaps in the Open Sea. *Journal of Physical Oceanography*, 16(2), 290–297. [https://doi.org/10.1175/1520-0485\(1986\)016<0290:SOBWOA>2.0.CO;2](https://doi.org/10.1175/1520-0485(1986)016<0290:SOBWOA>2.0.CO;2)

Horn, R., Nottensteiner, A., Reigber, A., Fischer, J., & Scheiber, R. (2009). F-SAR - DLR's new multifrequency polarimetric airborne SAR. *IEEE International Geoscience and Remote Sensing Symposium*. <https://doi.org/10.1109/IGARSS.2009.5418244>

Hsu, S. A., Meindl, E. A., & Gilhousen, D. B. (1994). Determining the power-law wind-profile exponent under near-neutral stability conditions at sea. *Journal of Applied Meteorology*, 33(6), 757–765. [https://doi.org/10.1175/1520-0450\(1994\)033<0757:DTPLWP>2.0.CO;2](https://doi.org/10.1175/1520-0450(1994)033<0757:DTPLWP>2.0.CO;2)

Hühnerfuss, H., Alpers, W., Dannhauer, H., Gade, M., Lange, P. A., Neumann, V., & Wismann, V. (1996). Natural and man-made sea slicks in the North Sea investigated by a helicopter-borne 5-frequency radar scatterometer. *International Journal of Remote Sensing*, 17(8), 1567–1582. <https://doi.org/10.1080/01431169608945364>

Hühnerfuss, H. A. G., Alpers, W., Theis, R., Wismann, V., & Lange, P. A. (1994). Classification of sea slicks by multifrequency radar techniques: New chemical insights and their geophysical implications. *Journal of Geophysical Research*, 99(C5), 9835–9845. <https://agupubs.onlinelibrary.wiley.com/doi/abs/10.1029/93JC03308>; <https://doi.org/10.1029/93JC03308>

Johansen, O., Reed, M., & Bodsberg, N. R. (2015, April). Natural dispersion revisited. *Marine Pollution Bulletin*, 93(1), 20–26. <https://doi.org/10.1016/j.marpolbul.2015.02.026>

Jones, C. E., Dagestad, K.-F., Breivik, Ø., Holt, B., Røhrs, J., Christensen, K. H., et al., (2016). Measurement and modeling of oil slick transport. *Journal of Geophysical Research: Oceans*, 121, 7759–7775. <https://doi.org/10.1002/2016JC012113>

Laxague, N. J. M., Özgökmen, T. M., Haus, B. K., Novelli, G., Shcherbina, A., Sutherland, P., et al., (2018). Observations of near-surface current shear help describe oceanic oil and plastic transport. *Geophysical Research Letters*, 45, 245–249. <http://doi.wiley.com/10.1002/2017GL075891>; <http://doi.org/10.1002/2017GL075891>

Leifer, I., Lehr, W. J., Simecek-Beatty, D., Bradley, E., Clark, R., Dennison, P., et al., (2012). State of the art satellite and airborne marine oil spill remote sensing: Application to the BP Deepwater Horizon oil spill. *Remote Sensing of Environment*, 124, 185–209. <http://www.sciencedirect.com/science/article/pii/S0034425712001563>; <https://doi.org/10.1016/j.rse.2012.03.024>

- Li, Z., Spaulding, M., French McCay, D., Crowley, D., & Payne, J. R. (2017). Development of a unified oil droplet size distribution model with application to surface breaking waves and subsea blowout releases considering dispersant effects. *Marine Pollution Bulletin*, 114(1), 247–257. <https://doi.org/10.1016/j.marpolbul.2016.09.008>
- Li, Z., Spaulding, M. L., & French-McCay, D. (2017). An algorithm for modeling entrainment and naturally and chemically dispersed oil droplet size distribution under surface breaking wave conditions. *Marine Pollution Bulletin*, 119(1), 145–152. <https://doi.org/10.1016/j.marpolbul.2017.03.048>
- Liu, Y., Macfadyen, A., Ji, Z.-G., & Weisberg, R. H. (2011). *Monitoring and modeling the deepwater horizon oil spill: A record-breaking enterprise*. Geophysical Monograph Series. American Geophysical Union (AGU). <https://doi.org/10.1029/GM195>
- Minchew, B., Jones, C. E., & Holt, B. (2012). Polarimetric analysis of backscatter from the Deepwater Horizon oil spill using L-band synthetic aperture radar. *IEEE Transactions on Geoscience and Remote Sensing*, 50(10), 3812–3830.
- Otremba, Z., & Piskozub, J. (2004). Modelling the bidirectional reflectance distribution function (BRDF) of seawater polluted by an oil film. *Optics Express*, 12(8), 1671–1676. <https://doi.org/10.1364/OPEX.12.001671>
- Reigber, A., Jäger, M., Pinheiro, M., Scheiber, R., Prats, P., Fischer, J., et al., (2012). Performance of the P-band subsystem and the X-band interferometer of the F-SAR airborne SAR instrument. *Paper presented in 2012 IEEE International Geoscience and Remote Sensing Symposium*. 5037–5040.
- Rigger, D. (1997). Edible oils: Are they really that different?. *International Oil Spill Conference Proceedings*, 1997(1), 59–61. <https://doi.org/10.7901/2169-3358-1997-1-59>
- Röhrs, J., & Christensen, K. H. (2015). Drift in the uppermost part of the ocean. *Geophysical Research Letters*, 42, 1–8. <https://doi.org/10.1002/2015GL066733>
- Röhrs, J., Christensen, K. H., Hole, L. R., Broström, G., Drivdal, M., & Sundby, S. (2012). Observation-based evaluation of surface wave effects on currents and trajectory forecasts. *Ocean Dynamics*, 62, 1519–1533. <https://doi.org/10.1007/s10236-012-0576-y>
- Röhrs, J., Dagestad, K.-F., Asbjørnsen, H., Nordam, T., Skancke, J., Jones, C. E., & Brekke, C. (2018). The effect of vertical mixing on the horizontal drift of oil spills. *Ocean Science*, 14, 1581–1601. <https://doi.org/10.5194/os-14-1581-2018>
- Schwartzberg, H. G. (1971). The movement of oil spills. *International Oil Spill Conference Proceedings*, 6, 489–494. <http://ioscproceedings.org/doi/abs/10.7901/2169-3358-1971-1-489>; <https://doi.org/10.7901/2169-3358-1971-1-489>
- Simecek-Beatty, D., & Lehr, W. J. (2017). Extended oil spill spreading with Langmuir circulation. *Marine Pollution Bulletin*, 122(1), 226–235. <https://doi.org/10.1016/j.marpolbul.2017.06.047>
- Skrunes, S., Brekke, C., & Doulgeris, A. P. (2015a). Characterization of low-backscatter ocean features in dual-copolarization SAR using log-cumulants. *IEEE Geoscience and Remote Sensing Letters*, 12(4), 836–840. <https://doi.org/10.1109/LGRS.2014.2363688>
- Skrunes, S., Brekke, C., & Eltoft, T. (2014). Characterization of marine surface slicks by Radarsat-2 multipolarization features. *IEEE Transactions on Geoscience and Remote Sensing*, 52(9), 5302–5319.
- Skrunes, S., Brekke, C., Eltoft, T., & Kudryavtsev, V. (2015b). Comparing near-coincident C- and X-band SAR acquisitions of marine oil spill. *IEEE Transactions on Geoscience and Remote Sensing*, 53(4), 1958–1975.
- Skrunes, S., Brekke, C., & Espeseth, M. M. (2017). Assessment of the RISAT-1 FRS-2 mode for oil spill observation. *Paper presented in 2017 IEEE International Geoscience and Remote Sensing Symposium (IGARSS)* (pp. 1024–1027). <https://doi.org/10.1109/IGARSS.2017.8127129>
- Skrunes, S., Brekke, C., Jones, C. E., & Holt, B. (2016). A multisensor comparison of experimental oil spills in polarimetric SAR for high wind conditions. *IEEE Journal of Selected Topics in Applied Earth Observations and Remote Sensing*, 9(11), 4948–4961. <https://doi.org/10.1109/JSTARS.2016.2565063>
- Sun, S., & Hu, C. (2019). The challenges of interpreting oil–water spatial and spectral contrasts for the estimation of oil thickness: Examples from satellite and airborne measurements of the Deepwater Horizon oil spill. *IEEE Transactions on Geoscience and Remote Sensing*, 57(5), 2643–2658.
- van der Mheen, M., Pattiaratchi, C., Cosoli, S., & Wandres, M. (2020). Depth-dependent correction for wind-driven drift current in particle tracking applications. *Frontiers in Marine Science*, 7, 305. <https://doi.org/10.3389/fmars.2020.00305>
- Wismann, V., Gade, M., Alpers, W., & Hühnerfuss, H. (1998). Radar signatures of marine mineral oil spills measured by an airborne multi-frequency radar. *International Journal of Remote Sensing*, 19(18), 3607–3623. <https://doi.org/10.1080/014311698213849>